MODELING THE SATURATED BIPOLAR TRANSISTOR

by

A.J. TREMBLAY, B.Sc.

A Thesis

Submitted to the School of Graduate Studies

in Partial Fulfillment of the Requirements

for the Degree

Master of Engineering

McMaster University

April 1981

MASTER OF ENGINEERING (1981) McMASTER UNIVERSITY

(Electrical Engineering) Hamilton, Ontario

TITLE: Modeling the Saturated Bipolar Transistor

AUTHOR: A.J. Tremblay, B.Sc. (Acadia University)

SUPERVISORS: Dr. S.H. Chisholm

Dr. H.D. Barber

NUMBER OF PAGES: xiii, 85

ABSTRACT

In this paper an analysis of the saturated bipolar transistor is presented, in the situation where the dc collector current is zero or close to zero. In this particular case, the device is referred to as a zero-biased transistor (ZBT). The analysis is based on a version of the integral charge-control model of Gummel and Poon.

Through analytic solution of the model equations and computer simulation, the dc collector-emitter voltage, small-signal collector-emitter conductance, and second and third-order nonlinear distortion are examined over a wide range of base currents. Both the ac and dc characteristics are found to be dominated by different physical phenomena at different levels of I_B. The effects of the parasitic substrate transistors on device operation are also examined. Criteria for acceptable performance are established with a view towards practical applications.

A number of applications for the ZBT have been suggested, particularly where a low-power small-signal variable-impedance element is required. Performance of the device in a small-signal attenuator and a feedback amplifier are discussed. The effects of a fixed parallel resistance and a finite base-drive impedance on device performance are investigated.

The results are found to describe the measured dc behaviour at low and moderate base currents for a family of lateral p-n-p transistors having symmetric forward and reverse-active properties. Similarly, low-frequency ac behaviour is well described at low and moderate base currents. Suggestions for future work are included.

ACKNOWLEDGEMENTS

The author wishes to express his sincere gratitude to Dr. S.H. Chisholm and to Dr. H.D. Barber for their guidance and supervision throughout the course of this work.

The devices used in this study were specially manufactured by Linear Technology Inc., of Burlington, Ontario. The courtesy of Dr. H.D. Barber, Vice-President, Operations, in providing samples of these devices is gratefully acknowledged.

The author is grateful to the Natural Sciences and Engineering Research Council of Canada and to McMaster University for their financial assistance.

Special thanks are due Mr. G. Kappel, who prepared the illustrations and Mrs. Betty Petro of the Word Processing Centre, who prepared the text.

TABLE OF CONTENTS

LIST OF ILLUSTRATIONS

LIST OF TABLES

LIST OF SYMBOLS

b	Ratio β_F/β_R
C	$\exp(v_{CB}/V_T)$
C_2	Forward low-current nonideal base current coefficient
C_4	Reverse low-current nonideal base current coefficient
$C_{jC}(0)$	Zero-bias collector-base junction capacitance
$C_{jE}(0)$	Zero-bias emitter-base junction capacitance
$C_{jS}(0)$	Zero-bias substrate-base junction capacitance
c_π	Nonlinear small-signal capacitance due to q_E
c_μ	Nonlinear small-signal capacitance due to q_C
c_{SUB}	Nonlinear small-signal capacitance due to q_{SUB}
E	$\exp(v_{EB}/V_T)$
e_o	Value of E/C for $I_C = 0$
g_{eco}	Small-signal collector-emitter conductance for $I_C = 0$
g_f, g_r, g_π, g_μ	First-order small-signal conductances of the nonlinear small-signal transistor model
g_{sr}, g_{sf}	First-order small-signal conductances due to the parasitic substrate transistors
g_2	Second-order coefficient of the Taylor series expansion for i_c
g_3	Third-order coefficient of the Taylor series expansion for i_c
H_1	First-order small-signal transfer function
H_2	Second-order small-signal transfer function
H_3	Third-order small-signal transfer function

HD_2	Fractional second harmonic distortion
HD_3	Fractional third harmonic distortion
I_B	DC component of i_B
I_C	DC component of i_C
I_E	DC component of i_E
I_{BL}	Break-point current, defined by (3.15)
I_{CC}	Reference collector source current
I_{EC}	Reference emitter source current
I_{CT}	Effective transported component of the collector current
I_K	Forward knee current
I_{KR}	Reverse knee current
I_{KS}	Substrate knee current
I_S	Saturation current
I_{SS}	Saturation current of the parasitic substrate transistors
I_{SBE}	Contribution of the substrate-base-emitter parasitic transistor to the base current
I_{SBC}	Contribution of the substrate-base-collector parasitic transistor to the base current
I_{STC}, I_{STE}	Effective transported components of the substrate current
i_B	Large-signal base current
i_C	Large-signal collector current
i_E	Large-signal emitter current
i_{SUB}	Large-signal substrate current
i_b	Small-signal base current
i_c	Small-signal collector current
i_{sub}	Small-signal substrate current

k	Boltzmann's constant
m_C	Collector-base grading coefficient
m_E	Emitter-base grading coefficient
m_{SUB}	Substrate-base grading coefficient
n_E	Nonideal low-current emitter-base emission coefficient
n_C	Nonideal low-current collector-base emission coefficient
q	Electronic charge
q_b	Gummel charge
q_C	Stored charge associated with the collector-base region
q_E	Stored charge associated with the emitter-base region
q_{bSE}	Gummel charge of the substrate-base-emitter parasitic transistor
q_{bSC}	Gummel charge of the substrate-base-collector parasitic transistor
R_B	Base ohmic resistance
R_C	Collector ohmic resistance
R_E	Emitter ohmic resistance
R_S	Substrate ohmic resistance
r_{eco}	Open-collector small-signal collector-emitter resistance
r_{ceo}	Open-emitter small-signal emitter-collector resistance
S	$\exp(v_{SB}/V_T)$
T	Temperature
V_A	Forward Early voltage
V_B	Reverse Early voltage
V_{EB}	DC base-emitter voltage
V_{EB}^*	External dc base-emitter voltage

V_{EC}	DC collector-emitter voltage
V_{ECO}	DC collector-emitter voltage with the collector open-circuited
V_T	Thermal voltage
v_{CB}	Large-signal base-collector voltage
v_{EB}	Large-signal base-emitter voltage
v_{SB}	Large-signal base-substrate voltage
v_{ec}	Small-signal collector-emitter voltage
v_{eco}	Small-signal collector-emitter voltage for $I_C = 0$
x	Ratio v_{ec}/V_T
β_F	Ideal forward current gain
β_R	Ideal reverse current gain
β_{RS}	Ideal reverse current gain of the parasitic substrate transistors
ϕ_C	Base-collector potential
ϕ_E	Base-emitter potential
ϕ_{SUB}	Base-substrate potential
τ_F	Forward transit time
τ_R	Reverse transit time

INTRODUCTION

One of the criteria for a good model of the bipolar junction transistor is that it successfully represent the device in all modes of operation. Such a model, based on a clear physical understanding of device behaviour, is an invaluable tool for evaluating performance and exploring new, possibly unconventional uses.

This paper focuses on the modeling and understanding of the bipolar transistor in the saturation mode, and in particular in the situation where the dc collector current is zero or close to zero. In this particular case the device is referred to as a zero-biased transistor (ZBT). Both dc and ac performance are examined, with a view towards practical applications.

The ZBT is of primary interest as a current-controlled small-signal variable impedance element. Other active devices, namely p-n junction diodes, Schottky barrier diodes, junction gate field-effect transistors and metal-oxide semiconductor transistors have been used for this purpose [1], [2]. To date, however, the possibilities of bipolar transistors as variable gain elements seem to have remained uninvestigated.

Variable gain elements are not easily realized in low-voltage micropower integrated circuits. On such single-chip devices space is at a premium, and the ability to obtain several decades of continuously variable small-signal resistance with a single transistor is of enormous

benefit. Furthermore, it can be easily fabricated alongside other bipolar circuitry.

The following chapter discusses the structure of the devices used in this study and the model used to represent them. Chapter Two outlines the techniques used to obtain the model parameters. Due consideration must be given to the dc properties of the ZBT and possible dc interaction with external circuitry; these topics are discussed in the third chapter. Chapter Four examines the ac properties of the ZBT, including small-signal resistance and nonlinear distortion.

CHAPTER 1

Device Structure and Models

The devices studied in this paper reflect their intended application as variable gain elements. Of central interest is a type of lateral p-n-p transistor having closely matched forward and reverse-active mode characteristics. These devices, designated Q009, were specially manufactured by Linear Technology Inc. The advantages of their symmetry will be made apparent in Chapter Four. In Chapters Three and Four theoretical study is made of a hypothetical device Q1 having parameters selected to be typical of ordinary (i.e. $\beta_F >> \beta_R$) integrated p-n-p transistors (such as the RCA CA3096E p-n-p).

1.1 Device Structure

The topology of the Q009 is shown in Figures 1.1(a) and (b). The grid structure, consisting of alternating collector and emitter segments, provides the desired symmetry between forward and reverse mode characteristics. This differs from conventional lateral p-n-p devices, where the emitter is surrounded by a ring-shaped collector region. As in any lateral p-n-p, additional parasitic p-n-p structures are formed between the collector, n-type base region, and the p-type substrate, and between the emitter, base, and substrate. These structures can affect device operation, and must be considered in any complete model.

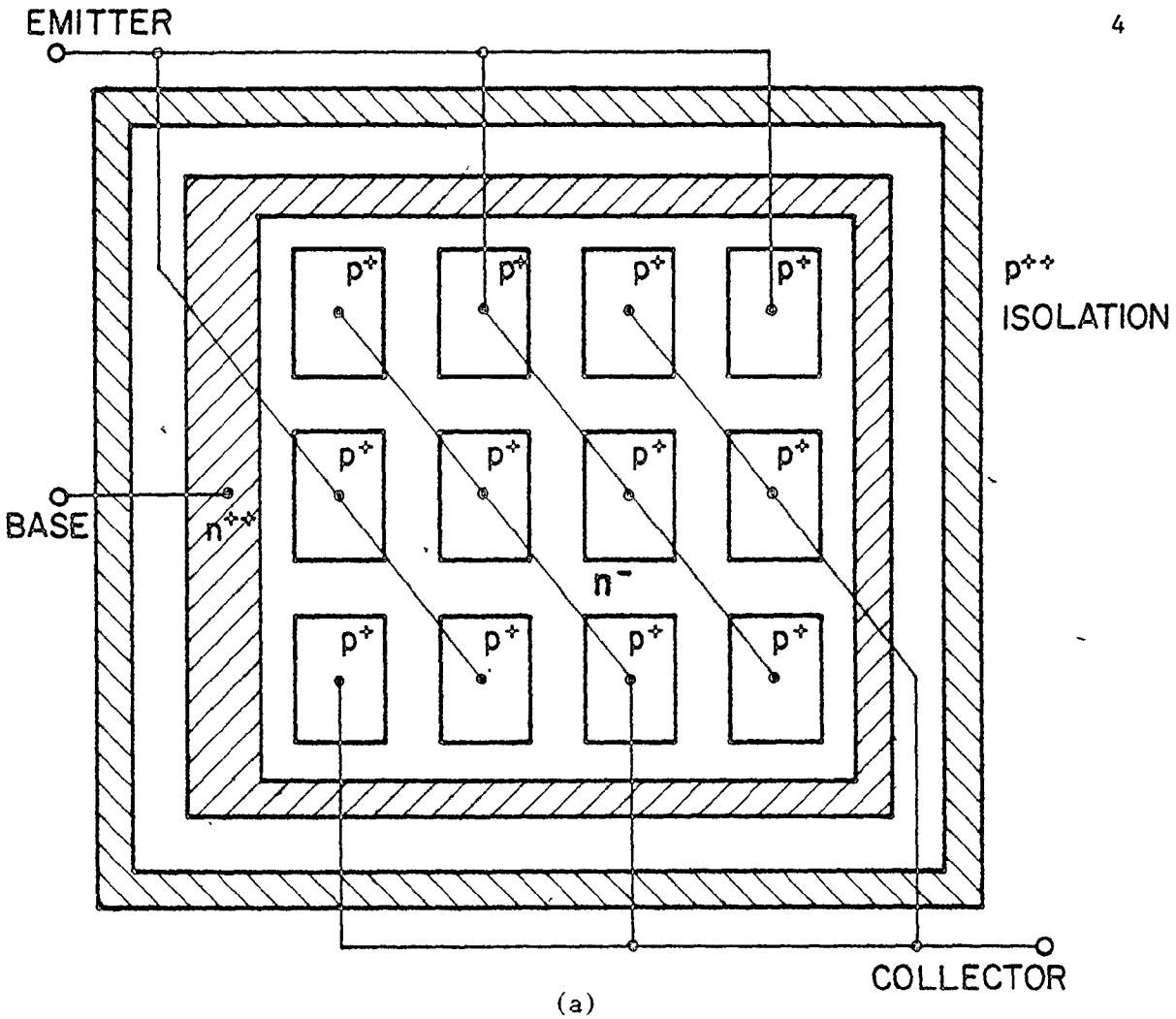

(a)

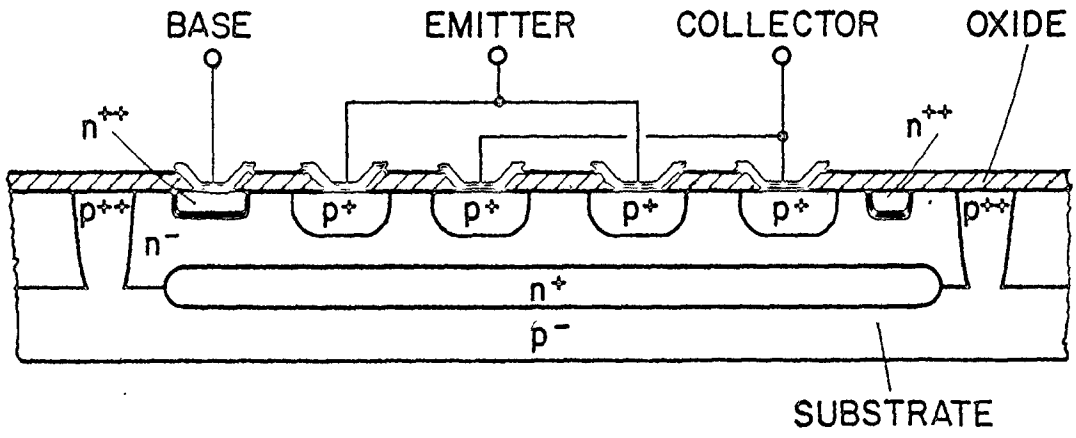

(b)

Figure 1.1. Topology of the symmetric lateral p-n-p transistor, Q009. (a) Top view. (b) Cross-section.

1.2 Three-Terminal Device Model

The bipolar transistor model used in this study is a modified version of the integral charge-control model of Gummel and Poon [3], as contained in the circuit simulation program SPICE [4], [5]. With reference to Figure 1.2, the effective transported component of the collector current is defined by

$$I_{CT} = \frac{1}{q_b} (I_{CC} - I_{EC}), \tag{1.1}$$

where

$$I_{CC} = I_S \left[\exp \left(\frac{v_{EB}}{V_T}\right) - 1\right] \tag{1.2}$$

$$I_{EC} = I_S \left[\exp \left(\frac{v_{CB}}{V_T}\right) - 1\right] \tag{1.3}$$

$$q_b = \frac{q_1}{2} + \left[\left(\frac{q_1}{2}\right)^2 + q_2\right]^{1/2} \tag{1.4a}$$

$$q_1 = 1 + \frac{v_{CB}}{V_A} + \frac{v_{EB}}{V_B} \tag{1.4b}$$

$$q_2 = \frac{I_S}{I_K} \left[\exp \left(\frac{v_{EB}}{V_T}\right) - 1\right] + \frac{I_S}{I_{KR}} \left[\exp \left(\frac{v_{CB}}{V_T}\right) - 1\right] . \tag{1.4c}$$

V_T is the thermal voltage kT/q and I_S is the saturation current parameter; V_A and V_B characterize forward and reverse mode basewidth modulation (the Early effect); I_K and I_{KR} are parameters ("knee"

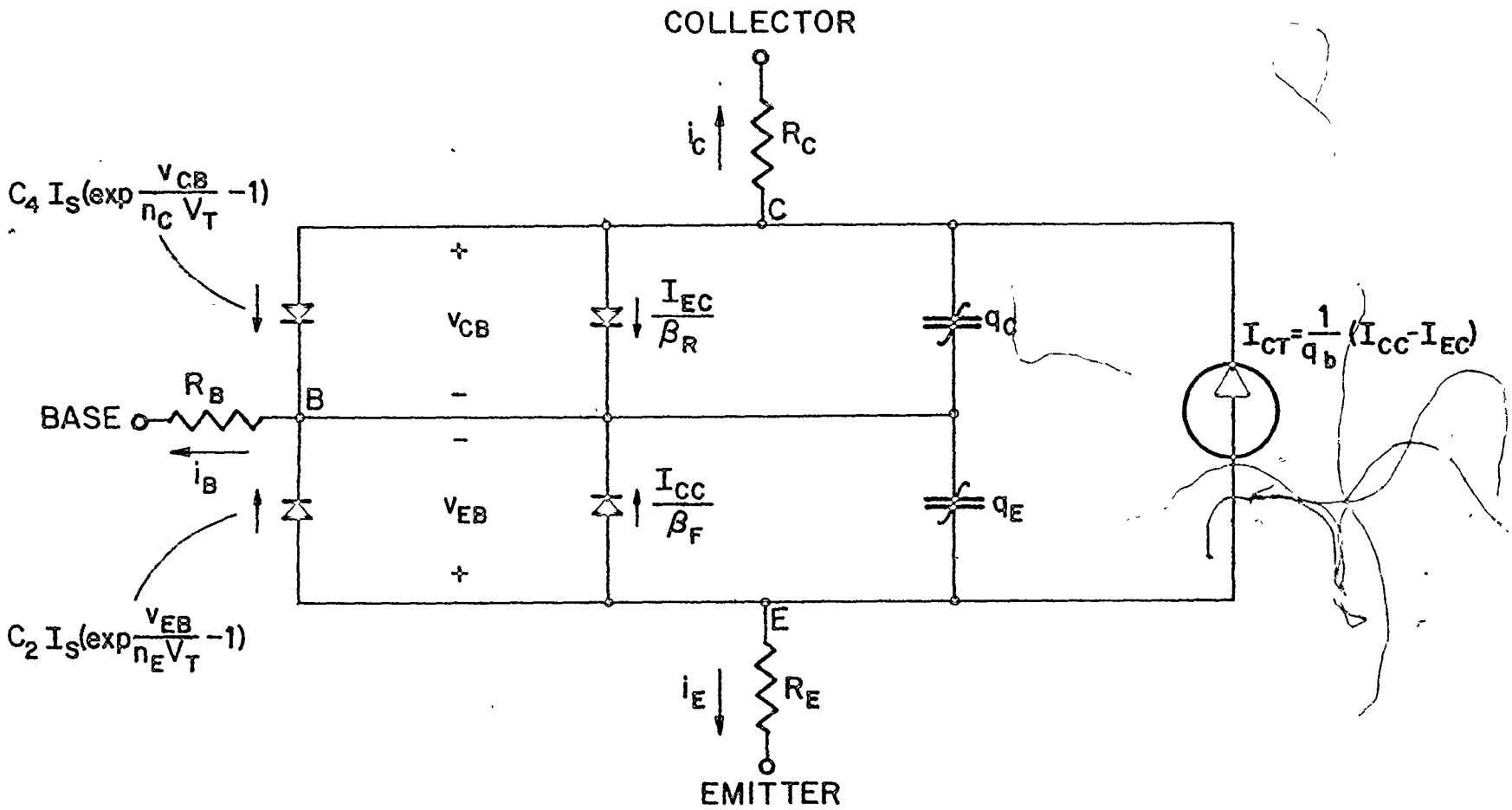

Figure 1.2. Large-signal model of the bipolar junction transistor (shown for a p-n-p transistor).

currents) characterizing high-level injection effects in forward and reverse mode operation; q_b is the normalized base majority charge (Gummel charge). The total collector terminal current is then given by

$$i_C = \frac{I_S}{q_b}\left[\exp\left(\frac{v_{EB}}{V_T}\right) - \exp\left(\frac{v_{CB}}{V_T}\right)\right]$$

$$- \frac{I_S}{\beta_R}\left[\exp\left(\frac{v_{CB}}{V_T}\right) - 1\right]$$

$$- C_4 I_S \left[\exp\left(\frac{v_{CB}}{n_c V_T}\right) - 1\right], \qquad (1.5)$$

while the total base terminal current is given by

$$i_B = \frac{I_S}{\beta_F}\left[\exp\left(\frac{v_{EB}}{V_T}\right) - 1\right] + C_2 I_S \left[\exp\left(\frac{v_{EB}}{n_E V_T}\right) - 1\right]$$

$$+ \frac{I_S}{\beta_R}\left[\exp\left(\frac{v_{CB}}{V_T}\right) - 1\right] + C_4 I_S \left[\exp\left(\frac{v_{CB}}{n_C V_T}\right) - 1\right], \qquad (1.6)$$

where β_F and β_R are the ideal forward and reverse current gains; n_E and C_2 characterize a nonideal diode modeling the effects of carrier recombination within the emitter-base space-charge region and at the surface, which dominates the base current under conditions of low forward bias [7], [8]. Similarly, n_C and C_4 characterize recombination inside, and at the surface of, the collector-base space-charge region. Three ohmic resistances R_C, R_B, and R_E are included in the model, and are taken to be constant.

Time and frequency-dependent device behaviour are modeled by the

nonlinear charge-storage elements q_E and q_C [9], given by

$$q_E = \tau_F I_S \left[\exp\left(\frac{v_{EB}}{V_T}\right) - 1\right] + C_{jE}(0) \int_0^{v_{EB}} \frac{dv}{(1 - v/\phi_E)^{m_E}} \tag{1.7}$$

$$q_C = \tau_R I_S \left[\exp\left(\frac{v_{CB}}{V_T}\right) - 1\right] + C_{jC}(0) \int_0^{v_{CB}} \frac{dv}{(1 - v/\phi_C)^{m_C}} \tag{1.8}$$

where τ_F and τ_R are the forward and reverse transit times, respectively, and $C_{jE}(0)$ and $C_{jC}(0)$ are the emitter-base and collector-base small-signal depletion layer capacitances, respectively, for zero dc junction voltage. Parameters m_E, ϕ_E, m_C and ϕ_C characterize the variation of these capacitances as a function of the junction voltages; ϕ_E and ϕ_C are the barrier potentials of the emitter-base and collector-base junctions, respectively; m_E and m_C depend on the impurity doping profiles of the respective junctions.

The model diagram in Figure 1.2 is drawn for a p-n-p transistor. Terminal currents flowing out of the device are taken to be positive. For an n-p-n transistor the voltage polarities of the internal elements and the reference current directions are reversed. In both cases all model parameter values are considered to be positive.

Models of the type used here enable the required parameters to be obtained directly from measurements at the transistor terminals. Devices can also be modeled by assigning separate diodes to the various internal injection currents. This approach can be used to examine arbitrary two or three dimensional structures, such as merged transistor logic (MTL) devices [10]. While providing valuable insight into the physical mechanisms responsible for device behaviour, the utility of such models is limited by the inaccessibility of the required input parameters, which must be determined from measurements of internal geometry and doping levels or of specially fabricated test devices. In the case of lateral p-n-p transistor, a one dimensional model similar in form to that of Gummel and Poon has been found to adequately describe dc active mode behaviour [11]. In cases where two dimensional effects are encountered, they can usually be treated by adding elements to the basic model. Such a case is considered in the next section.

1.3 Inclusion of the Substrate

The parasitic p-n-p transistors can be readily incorporated into the existing device model [6], [12]. With reference to Figure 1.3(a), QA represents the lateral p-n-p device, QSE is the parasitic p-n-p formed between the emitter, base, and substrate, and QSC is that formed between the collector, base, and substrate. The substrate is defined as the collector of QSE and QSC, as in most circuit applications it is at a lower potential than the other three terminals. Note that the emitter-base junction of QSC and the collector-base junction of QA are

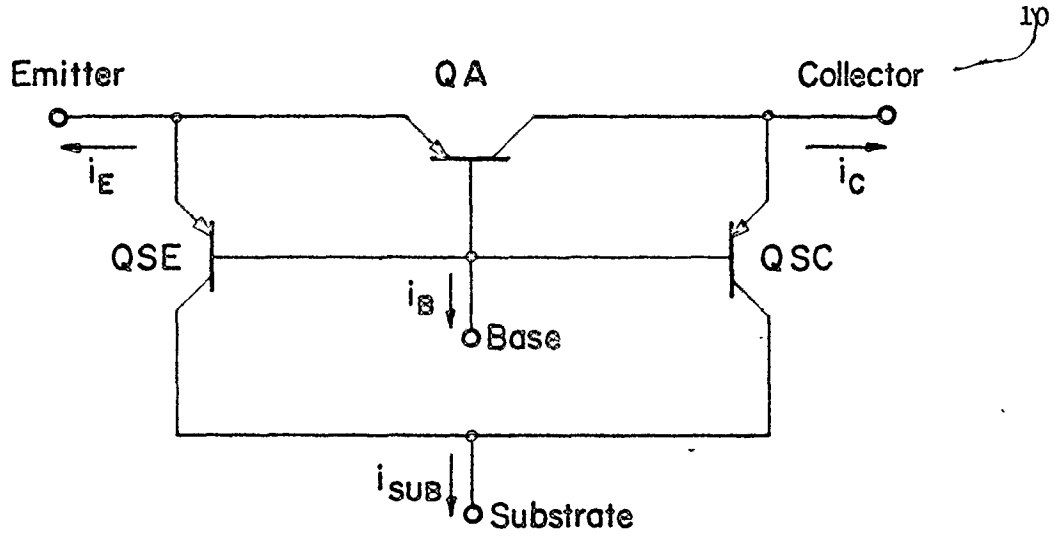

(a)

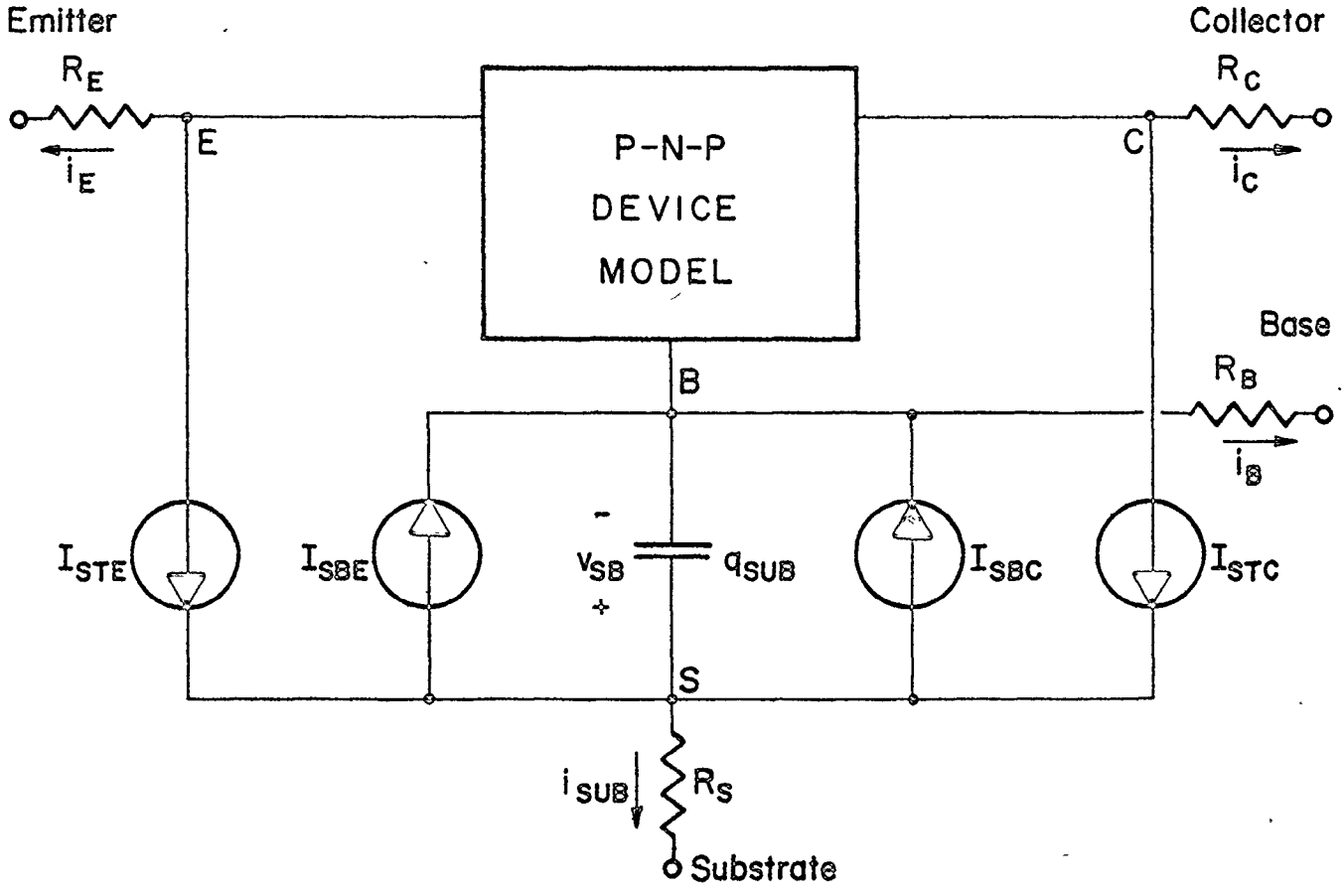

(b)

Figure 1.3. The p-n-p device model with the parasitic substrate transistors included. (a) Three-transistor equivalent model. (b) Components added to existing device model.

physically the same junction, and must not be modeled twice. When using the program SPICE this is readily accomplished by giving β_F a very large value (say 10^7) for QSC, effectively eliminating its contribution to the base current. The same comments apply to the emitter-base junctions of QA and QSE.

Due to the symmetric structure of the Q009, the parameters of QSE and QSC are taken to be identical. Referring to Figure 1.3(b), the effective transported components of the substrate current i_{SUB} are

$$I_{STE} = \frac{I_{SS}}{q_{bSE}} \left[\exp\left(\frac{v_{EB}}{V_T}\right) - \exp\left(\frac{v_{SB}}{V_T}\right)\right] \tag{1.9}$$

$$I_{STC} = \frac{I_{SS}}{q_{bSC}} \left[\exp\left(\frac{v_{CB}}{V_T}\right) - \exp\left(\frac{v_{SB}}{V_T}\right)\right] \tag{1.10}$$

with

$$q_{bSE} = \left\{\frac{I_{SS}}{I_{KS}} \left[\exp\left(\frac{v_{EB}}{V_T}\right) - 1\right]\right\}^{1/2} \tag{1.11}$$

$$q_{bSC} = \left\{\frac{I_{SS}}{I_{KS}} \left[\exp\left(\frac{v_{CB}}{V_T}\right) - 1\right]\right\}^{1/2} . \tag{1.12}$$

I_{SS} is the saturation current parameter for the parasitic transistors; I_{KS} models high-level injection for these devices. The currents I_{SBE} and I_{SBC} represent the contribution of the substrate to the base terminal current. Each consists of an ideal component and a low-current recombination component, similar in form to those of (1.6). For example, the ideal component of I_{SBE} and I_{SBC} is given by

$$I_{SBE(ideal)} = I_{SBC(ideal)} = \frac{I_{SS}}{\beta_{RS}} \left[\exp\left(\frac{v_{SB}}{V_T}\right) - 1\right], \qquad (1.13)$$

where β_{RS} is defined as the ideal reverse current gain of the parasitic transistors. Similarly, parameters can be defined to characterize the recombination component. The contribution of I_{SBE} and I_{SBC} to the total base current will be negligible when the substrate-base junction is reverse biased. Finally, an ohmic resistance R_{SUB} and a charge-storage element q_{SUB} are included; the latter is given by

$$q_{SUB} = C_{jS}(0) \int_0^{v_{SB}} \frac{dv}{(1 - v/\phi_{SUB})^{m_{SUB}}}, \qquad (1.14)$$

where $C_{jS}(0)$ is the substrate-base depletion layer capacitance at zero junction voltage, ϕ_{SUB} is the barrier potential, and m_{SUB} is the junction grading coefficient.

It should be noted that the symmetry between the parasitic devices does not limit the generality of the model outlined in Figure 1.3(b). Where warranted, different parameters can be ascribed to the two substrate p-n-p's, and determined using the terminal measurement techniques outlined in the next chapter.

CHAPTER 2

Measurement of Model Parameters

Many of the techniques used to measure model parameters closely follow those outlined by Getreu [6]. Devices under test were placed in a shielded enclosure; ambient temperature was held to 22.5 $\pm$ 1°C.

The dc forward mode characteristics, with the exception of the Early voltage, were obtained using the circuit of Figure 2.1, with $v_{CB} = v_{SB} = 0$. Under this condition, equations (1.5), (1.6), (1.9) - (1.13), and Figure 1.3(b) yield

$$i_c = I_C = \frac{I_S}{q_b} \exp\left(\frac{v_{EB}}{V_T}\right) \tag{2.1}$$

$$i_B = I_B = \frac{I_S}{\beta_F}\left[\exp\left(\frac{v_{EB}}{V_T}\right) - 1\right] + C_2 I_S\left[\exp\left(\frac{v_{EB}}{n_E V_T}\right) - 1\right] \tag{2.2}$$

$$i_{SUB} = I_{SUB} = \frac{I_{SS}}{q_{bSE}}\left[\exp\left(\frac{v_{EB}}{V_T}\right) - 1\right]. \tag{2.3}$$

For low-level injection $q_b \approx 1$, and the intercept of $\ln(I_C)$ versus V_{EB} curve is simply $\ln(I_S)$. Similarly, the intercept of the $\ln(I_{SUB})$ versus V_{EB} curve yields I_{SS}. At low currents, I_B is dominated by the second term of (2.2); from the $\ln(I_B)$ measurements in this region C_2 and n_E are obtained. As I_B increases, the first term of (2.2) dominates, yielding

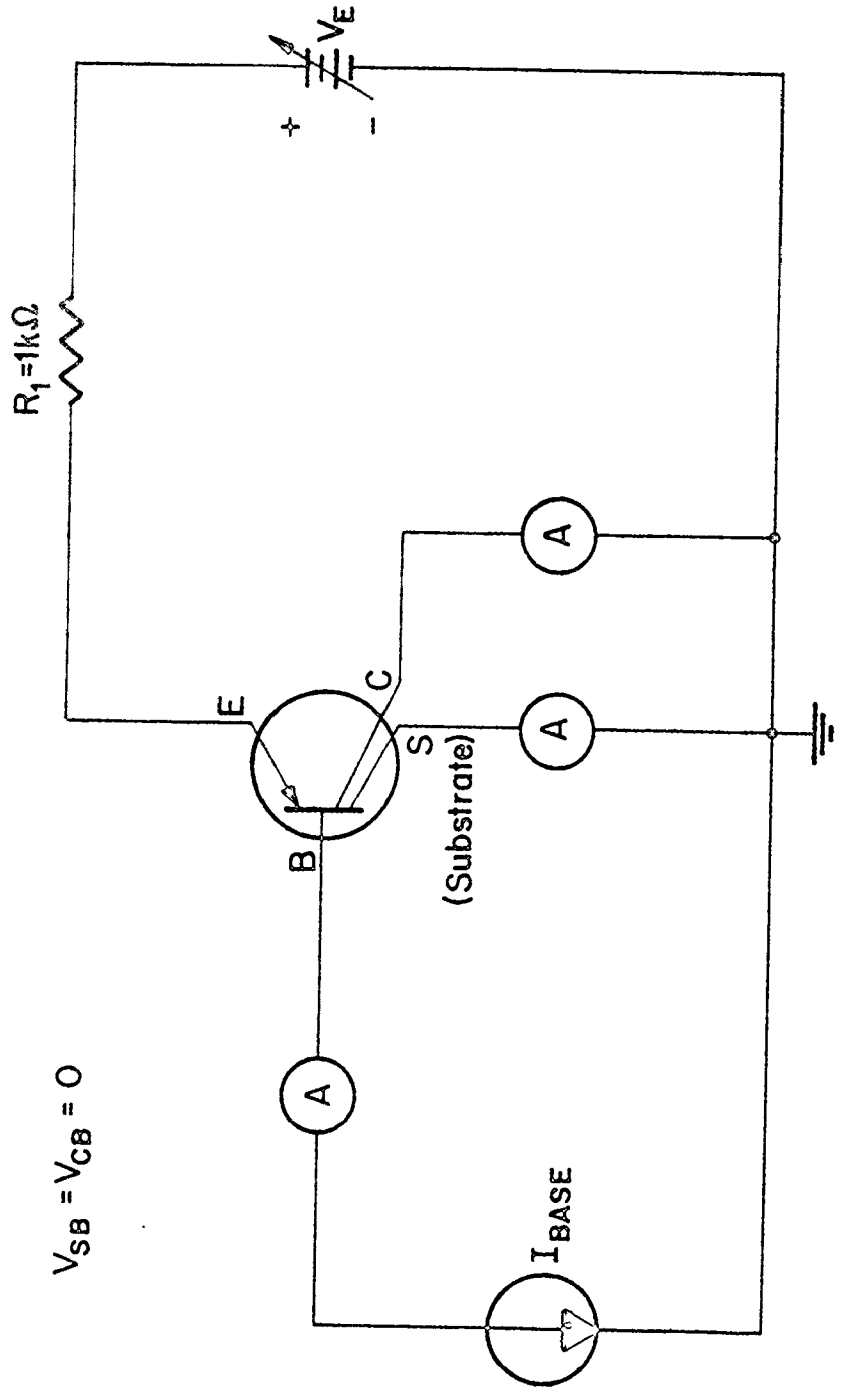

Figure 2.1. Test circuit used to measure the dc model parameters.

β_F. Measured I_B characteristics in this region often have slopes close to, but not identical to, q/kT. This may be due to current crowding in the base region [13] or the onset of other high-current effects not incorporated in the SPICE version of the Gummel-Poon model. In general, a very close fit of the measured characteristics to (2.2) can be obtained by setting β_F equal to the maximum value of I_C/I_B. At high currents the externally measured emitter-base voltage V_{EB}^*, defined by

$$V_{EB}^* = V_{EB} + I_B R_B + I_E R_E \quad , \tag{2.4}$$

must be corrected to allow for the ohmic voltage drops across R_B and R_E [6]. When this is done, the intercept of the high and low-current asymptotes of $\ln(I_C)$ define the knee current I_K. Similarly, when the $\ln(I_{SUB})$ versus V_{EB} curve is corrected for the voltage drops across R_E and R_C, the high and low-current asymptotes define I_{KS}.

Figure 2.2 depicts the $\ln(I_C)$, $\ln(I_B)$, and $\ln(I_{SUB})$ versus V_{EB} characteristics of a typical sample of the Q009 device. All terminal voltage and current measurements were made using a Keithley Model 610 electrometer, except at very high currents, where they were displayed on the CRT of a Tektronix Type 576 curve tracer. Below 10 nA base currents were provided by a dc power supply in series with 10^{10} or 10^{11} ohm 1% resistors; above 10 nA the calibrated base current source of the Tektronix Type 576 curve tracer was used. The latter was operated in a pulsed mode at very high current levels in order to avoid internal heating in the device; the pulses were of 300 μs duration. From a similar set of measurements, made with the positions of the collector

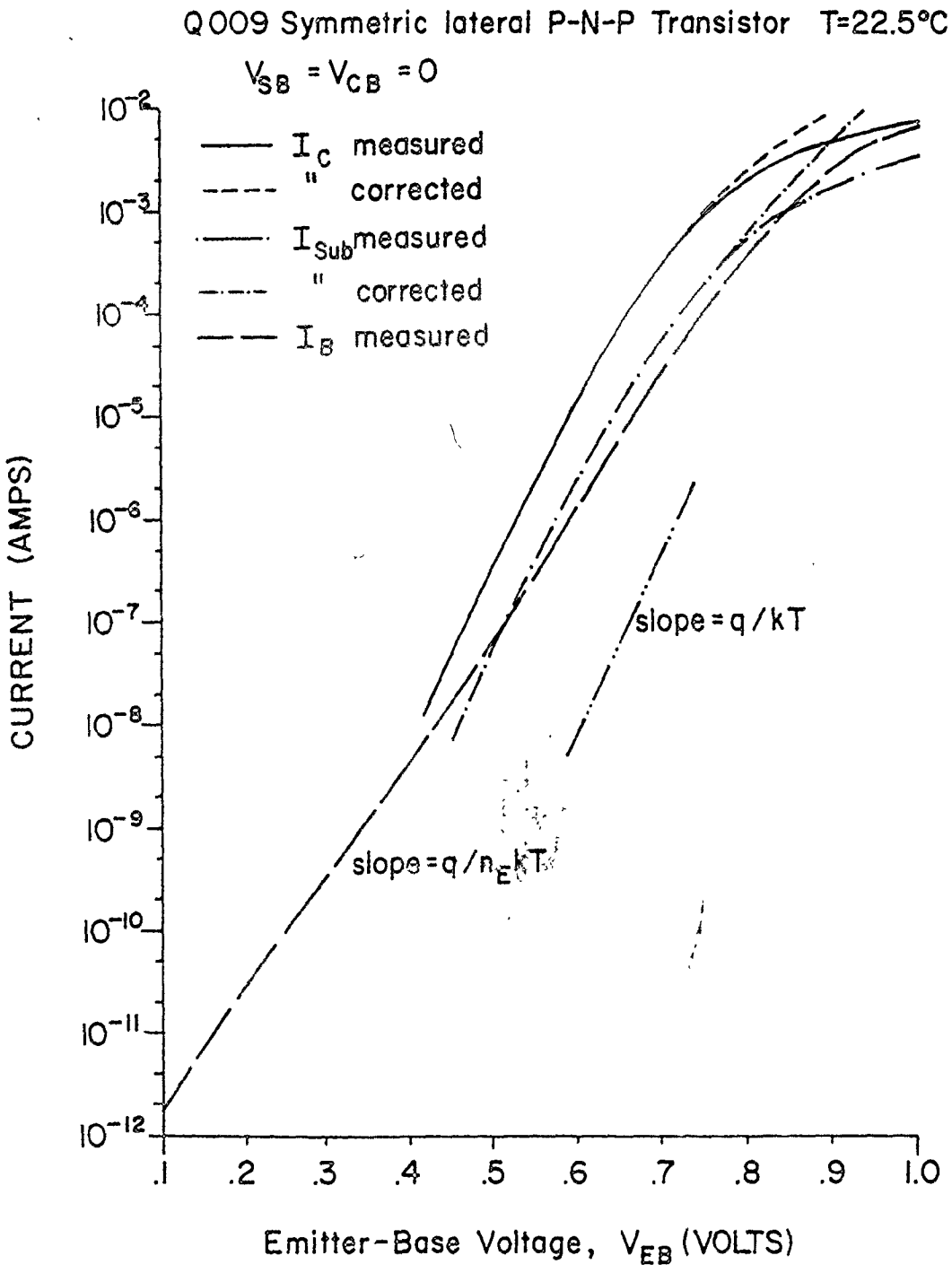

Figure 2.2. Measured ln (I_C), ln (I_B) and ln (I_{SUB}) versus V_{EB} characteristics for the Q009 transistor.

and emitter terminals in Figure 2.1 interchanged, the parameters C_4, n_C, β_R, and I_{KR} were obtained.

With the emitter and collector grounded and a positive bias applied to the substrate, the parameters modeling the contribution of the substrate to the base terminal current can be determined. For example, if I_{SUB} is sufficiently large that the recombination term of this contribution can be neglected, equations (1.5), (1.6), (1.9) - (1.13) and Figure 1.3(b) yield, for $v_{EB} = v_{CB} = 0$,

$$I_C = \frac{I_{SS}}{q_{bSE}} \left[\exp\left(\frac{v_{SB}}{V_T}\right) - 1\right] \tag{2.5}$$

$$I_B = \frac{2I_{SS}}{\beta_{RS}} \left[\exp\left(\frac{v_{SB}}{V_T}\right) - 1\right] . \tag{2.6}$$

In the absence of high-level injection, $q_{bSE} = 1$, and the ratio of I_C to I_B is $\beta_{RS}/2$. Under the same conditions at very low currents, I_B is dominated by the recombination terms of the parasitic transistors; the $\ln(I_B)$ versus V_{SB} characteristic in this region yields the corresponding model parameters. The latter were not determined for the Q009 device, since the measured base currents were found to follow (2.6) down to values of 1 nA.

The emitter series resistance is frequently measured using an open-circuited collector method, with a related forced-beta method used to measure the collector series resistance [14]. This technique requires measurement at very high base currents, often in excess of 10 mA, in order to obtain these parameters. For many of the transistors tested this was not found to be practical, due to problems associated

with internal heating and potential device destruction.

A computer-aided technique has been introduced by Incecik [15] which avoids these difficulties. However, it assumes that the Gummel-Poon model accurately predicts the open collector device behaviour at current levels where the voltage drops across R_C or R_E become significant. This was not found to be true for the Q009 device, and application of the computer-aided method resulted in strongly current-dependent resistance values. These ranged from over 100Ω at base currents below 100 μA to about 10Ω at 50 mA. Physically, such a variation cannot be correct since the series resistances of the highly doped emitter and collector regions of the symmetric p-n-p are virtually constant.

Although the computer-aided results asymptotically approached constant resistance values at high currents, a more definitive assessment of R_E and R_C was made using the small-signal circuit illustrated in Figure 2.3 (the operational amplifier is a National Semiconductor LF355N). At sufficiently high frequencies the blocking capacitor C_B behaves as a short circuit, and the voltage gain is given by

$$\frac{v_o}{v_i} = 1 + \frac{R_F}{r_{eco}} \quad , \tag{2.7}$$

where r_{eco} is the small-signal collector-emitter resistance of the transistor with $I_C = 0$. It consists of the internal device resistance, which is a function of base current, in series with R_E and R_C, which are assumed constant. As shown in Chapter Four, the internal component

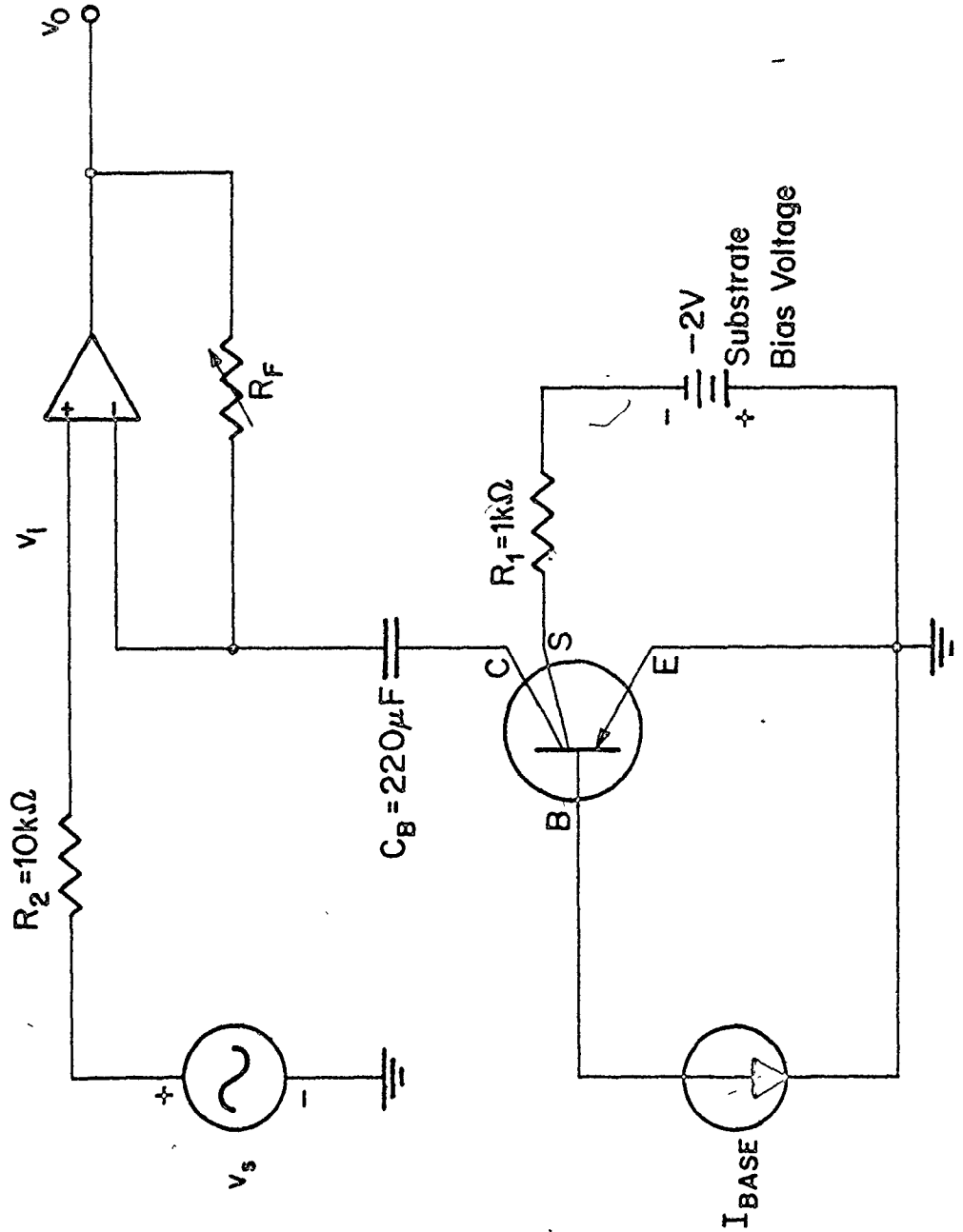

Figure 2.3. Test circuit used to measure the small-signal collector-emitter resistance r_{eco}.

becomes negligible at high currents, and r_{eco} asymptotically approaches $R_E + R_C$. Then, due to the symmetry of the Q009,

$$R_E = R_C = \frac{1}{2} r_{eco} \Big|_{I_B \to \infty} . \tag{2.8}$$

The r_{eco} versus I_B characteristics required for determining R_E and R_C were readily obtained using (2.7) by monitoring the voltage gain and R_F at each operating point. Grounding the substrate and biasing the emitter at -2V, $R_C + R_S$, and hence R_S, were obtained after a similar fashion. In all cases the input voltage v_i was maintained near 4 mV rms.

The base series resistance R_B is generally very difficult to measure. An estimate can be made using (2.4):

$$R_B = \frac{V_{EB}^* - V_{EB} - I_E R_E}{I_B} ; \tag{2.7}$$

the internal voltage drop V_{EB} lies on the ideal $\ln(I_B)$ characteristic of Figure 2.2 extrapolated into the high-current region.

Standard techniques were employed in measuring the Early voltages V_A and V_B, the forward and reverse transit times τ_F and τ_R, and the parameters modeling the junction small-signal capacitances $C_{jC}(v_{CB})$, $C_{jE}(v_{EB})$ and $C_{jS}(v_{SB})$. Details are given by Getreu [6].

The parameters obtained for a represenative sample of the Q009 transistor are listed in Table 2.1. Parameters relating to the parasitic transistors in the same device are shown separately in Table 2.2. Table 2.3 lists the model parameters of the hypothetical device

Q1, discussed in Chapter One. These were selected to be typical of conventional general-purpose lateral p-n-p's, and were obtained from manufacturers' specification sheets and actual measurements of a variety of transistors.

Table 2.1

Model Parameter Values for the Q009 Symmetric Lateral p-n-p Transistor

Parameter	Measured Value
β_F	14.58
β_R	15.14
I_S	1.34×10^{-15} A
R_B	7 Ω
R_C	4 Ω
R_E	4 Ω
V_A	60 V
V_B	60 V
I_K	6.5×10^{-4} A
I_{KR}	6.5×10^{-4} A
C_2	142
n_E	1.56
C_4	137
n_C	1.60
τ_F	37.9 ns
τ_R	31.8 ns
$C_{jE}(0)$	0.909 pF
m_E	0.389
ϕ_E	0.5 V
$C_{jC}(0)$	0.981 pF
m_C	0.347
ϕ_C	0.5 V

Table 2.2

Model Parameter Values for the Parasitic Substrate Transistors of the Q009 Device

Parameter	Measured Values
β_{RS}	1.95×10^{-2}
I_{SS}	1.75×10^{-16} A
R_S	13 Ω
I_{KS}	9.0×10^{-5} A
$C_{jS}(0)$	4.11 pF
m_{SUB}	0.235
ϕ_{SUB}	0.5 V

Table 2.3

Model Parameters Selected for the Q1
p-n-p Transistor

Parameter	Measured Value
β_F	50
β_R	1
I_S	1.0×10^{-16} A
R_B	50 Ω
R_C	5 Ω
R_E	1 Ω
V_A	100 V
V_B	100 V
I_K	10 mA
I_{KR}	100 mA
C_2	100
n_E	1.75
C_4	5
n_C	1.75
τ_F	1 ns
τ_R	50 ns
$C_{jE}(0)$	1 pF
m_E	0.333
ϕ_E	0.7 V
$C_{jC}(0)$	3 pF
m_C	0.333
ϕ_C	0.5 V

CHAPTER 3

DC Characteristics of the Zero-Biased Transistor

In this chapter the dc characteristics of the ZBT are discussed; namely, the variation of the dc collector-emitter voltage V_{EC} as a function of the base current. A detailed knowledge of this behaviour is useful in predicting the dc interaction of the device with the concomitant circuitry, and permits the establishment of criteria for improved dc performance, based on the physical device properties.

3.1 Analytic Formulation

An exact solution for V_{EC} using the model equations of Chapter One requires numerical methods. While this is readily accomplished with the aid of a computer, it is possible, by making some simplifying assumptions, to obtain analytic expressions for V_{EC}. In addition to providing computational simplicity, they afford a means whereby the influence of the various device parameters on the observed behaviour can be directly assessed. As such they increase the understanding of the device and assist in determining design crtieria for improved performance.

From (1.5) $i_C = 0$ implies

$$\exp\left(\frac{v_{EB}}{V_T}\right) = -q_b\left(\frac{1}{\beta_R} + C_4\right) + \left(1 + \frac{q_b}{\beta_R}\right)\exp\left(\frac{v_{CB}}{V_T}\right)$$

$$+ q_b C_4 \exp\left(\frac{v_{CB}}{n_C V_T}\right) \quad . \tag{3.1}$$

The first term on the right hand side of (3.1) can be neglected, except when the junction voltages are close to V_T in magnitude. Note that $v_{EC} = v_{EB} - v_{CB}$ and let

$$C = \exp\left(\frac{v_{CB}}{V_T}\right) \tag{3.2}$$

$$E = \exp\left(\frac{v_{EB}}{V_T}\right) \tag{3.3}$$

$$V_{ECO} = v_{EC} \Big|_{i_C = 0} \tag{3.4}$$

$$e_o = \frac{E}{C}\Big|_{i_C = 0} = \exp\left(\frac{v_{ECO}}{V_T}\right) \quad . \tag{3.5}$$

Equation (3.1) can then be written as

$$e_o = \left(1 + \frac{q_b}{\beta_R}\right) + \frac{q_b C_4}{C^{(1-1/n_C)}} \quad . \tag{3.6}$$

The terms dominating (3.6) vary according to the base current level. At moderate levels the recombination term is insignificant, and, with the assumption of low-level injection, (3.6) reduces to

$$e_o = 1 + \frac{1}{\beta_R} \tag{3.7}$$

or

$$V_{ECO} = V_T \ln \left(1 + \frac{1}{\beta_R}\right) \quad . \tag{3.8}$$

This is the result obtained by Choma [14]. Note that V_{ECO} is independent of I_B. Similarly, with the device inverted and the emitter terminal open,

$$V_{CEO} = V_T \ln \left(1 + \frac{1}{\beta_F}\right) \quad , \tag{3.9}$$

where V_{CEO} is defined as the emitter-collector voltage with $i_E = 0$.

At increased currents the term q_b becomes significant, and (3.6) becomes

$$V_{ECO} = V_T \ln \left(1 + \frac{q_b}{\beta_R}\right) \quad . \tag{3.10}$$

The voltage drop across the emitter series resistance R_E must also be considered and hence the external emitter-collector voltage V_{ECO}^* across the device terminals is given by

$$V_{ECO}^* = V_{ECO} + I_B R_E \quad , \tag{3.11}$$

with V_{ECO} given by (3.10). If it is assumed that q_b correctly models high-level injection, it can be shown that the slope of the V_{ECO}^* versus I_B characteristic approaches R_E as I_B is increased, thereby affording a technique for measuring the emitter series resistance [14].

At low current levels the term $C^{(1-1/n_C)}$ of (3.6) becomes small, marking the onset of recombination effects. Hence, V_{ECO} rises above the

constant mid-current value given by (3.8). It is useful at this stage to analyze separately conventional and symmetric devices, for each of which a different set of simplifying approximations apply. For the conventional device, $\beta_F \gg \beta_R$ and $C_4 \gg C_2$; under these conditions (1.6) reduces to

$$i_B = I_B = \frac{I_S}{\beta_R} C + C_4 I_S C^{1/n_C} , \tag{3.12}$$

with $C \gg 1$. A comparison of (3.6) with (3.12) yields

$$e_o = 1 + \frac{I_B}{I_S C} , \tag{3.13}$$

with q_b taken to be unity. For most devices n_C is found to be approximately 2; this is consistent with the physical theory for carrier recombination in the space-charge layer [7], [16]. With $n_C=2$, (3.12) permits C to be expressed as a function of I_B:

$$C = \frac{\beta_R I_B}{I_S} \left\{1 + \frac{I_S C_4^2 \beta_R}{2I_B} \left[1 - \left(1 + \frac{4I_B}{C_4^2 \beta_R I_S}\right)^{1/2}\right]\right\} . \tag{3.14}$$

Let the break-point current I_{BL} be defined by

$$I_{BL} = I_S \beta_R C_4^2 . \tag{3.15}$$

(3.13) now becomes

$$e_o = 1 + \frac{1}{\beta_R} \left\{1 + \frac{I_{BL}}{2I_B} \left[1 - \left(1 + \frac{4I_B}{I_{BL}}\right)^{1/2}\right]\right\}^{-1} . \tag{3.16}$$

Note that I_{BL} is half the value of I_B, as given by (3.12), at which the recombination and ideal components are equal. For $I_B >> I_{BL}$, (3.16) collapses to (3.7), as expected. For $I_B << I_{BL}$, expansion of $(1 + 4I_B/I_{BL})^{1/2}$ yields

$$e_o \simeq \frac{1}{\beta_R} \frac{I_{BL}}{I_B} \quad , \tag{3.17}$$

or

$$V_{ECO} \simeq V_T \left[\ln \left(\frac{I_{BL}}{I_B}\right) + \ln \left(\frac{1}{\beta_R}\right)\right] \quad . \tag{3.18}$$

Thus, at very low currents the V_{ECO} versus ln I_B curve has a slope of $-V_T$. This rise in V_{ECO} with decreasing I_B does not continue indefinitely. When the junction voltages become comparable in magnitude to V_T, the $-(1/\beta_R + C_4)$ term of (3.1), neglected in this analysis, becomes significant, and eventually V_{ECO} is zero when $I_B = 0$.

For the symmetric device, the approximations made in obtaining (3.12) are no longer valid, and a simple analytic expression for e_o cannot be obtained. However, when the recombination terms dominate the base current, (1.6) reduces to

$$i_B = I_B \simeq C_2 I_S E^{1/n_E} + C_4 I_S C^{1/n_C} \quad . \tag{3.19}$$

With $C_2 = C_4 = C_B$ and $n_E = n_C = n$, this becomes

$$I_B = I_S C_B C^{1/n} \left[1 + \left(\frac{E}{C}\right)^{1/n}\right] \quad , \tag{3.20}$$

which for $i_C = 0$ becomes

$$I_B = I_S\, C_B\, C^{1/n}\, (1 + e_O^{1/n}) \quad . \tag{3.21}$$

Under the same conditions (3.6) may be written:

$$e_O \approx 1 + \frac{C_B}{C^{(1-1/n)}} \quad . \tag{3.22}$$

From (3.21) and (3.22) the following expression is obtained:

$$e_O = 1 + C_B \left(\frac{I_S\, C_B}{I_B}\right)^{n-1} \left(1 + e_O^{1/n}\right)^{n-1} \quad . \tag{3.23}$$

This is readily solved for e_O, and hence V_{ECO}, using iterative techniques. A solution for the Q009 device, with $C_B = 140$ and $n = 1.56$, is plotted in Figure 3.1. Again, V_{ECO} is seen to rise with decreasing base currents. If n=2 and $I_B \ll I_S\, C_B^{\,2}$, (3.23) reduces to

$$e_O \approx (I_S\, C_B^{\,2}/I_B)^2 \quad . \tag{3.24}$$

The slope of the V_{ECO} versus ln I_B characteristic is then $-2V_T$, twice that which was obtained for the conventional device at very low currents.

From the circuit design point of view, the rise in V_{ECO} at low base currents is of major consequence. First, modulation of the base current, such as that which might occur if the ZBT were employed as a small-signal variable gain element in a compression amplifier, produces a corresponding modulation of the collector-emitter voltage. Special precautions, such as capactive filtering, must then be taken to prevent such spurious fluctuations of V_{ECO} from affecting circuit performance.

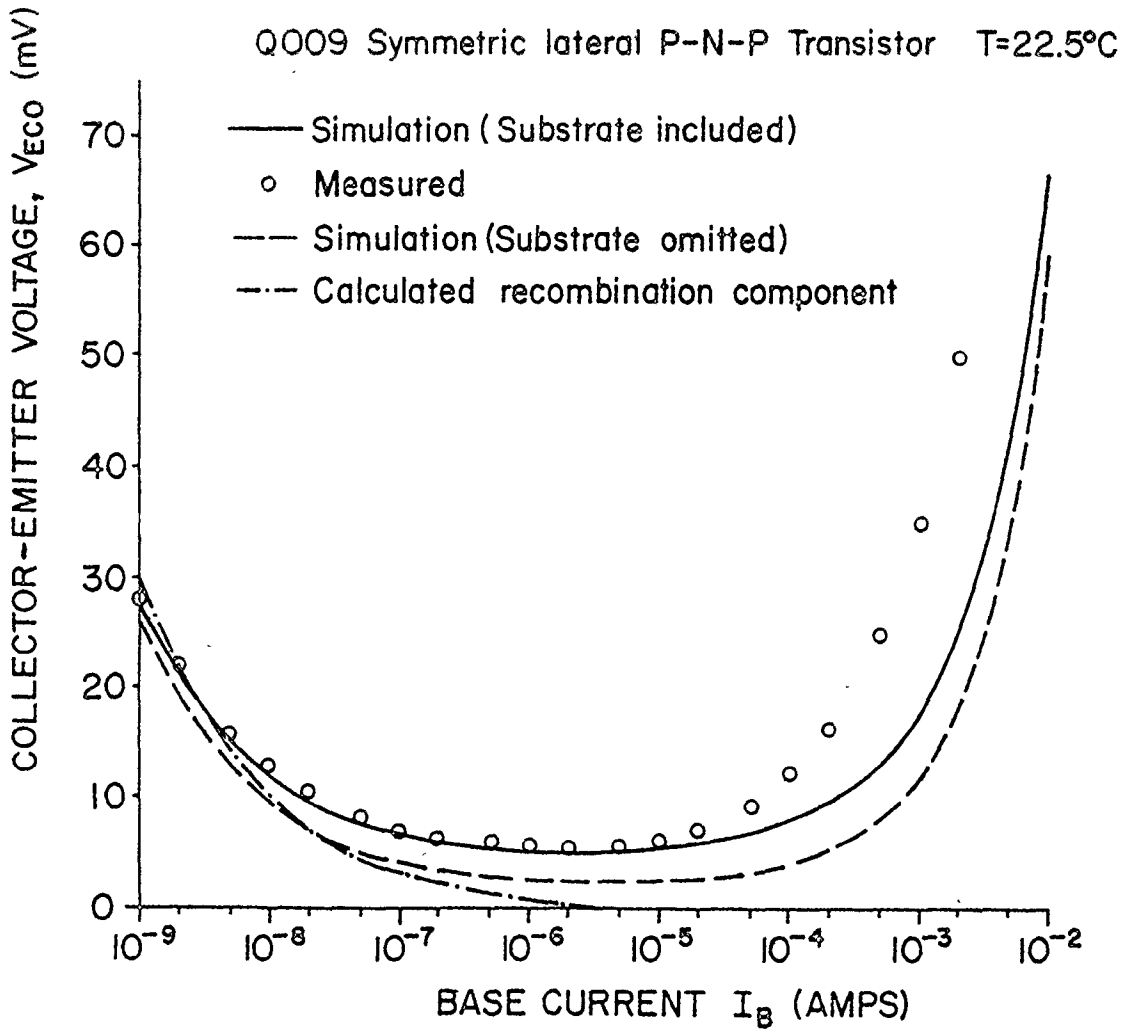

Figure 3.1. DC open-circuited collector-emitter voltage V_{ECO} of the Q009 transistor as a function of base current (substrate biased at -2V with respect to the emitter).

Second, a large dc voltage between the emitter and collector is in itself undesirable in cases where supply voltages are limited. Values of V_{ECO} commonly reach 100 - 200 mV at low currents. In hearing-aid or pacemaker circuits, for example, this represents a large fraction of the supply voltage, which is usually of the order of one or two volts.

From the discussion of conventional and symmetric devices at low base currents, it is clear that the break-point value of I_B, at which V_{ECO} begins to rise, is roughly proportional to C_B^2 (C_4^2 in the conventional device) for values of n near 2. Device processing efforts should be concentrated on ensuring that recombination effects are sufficiently low that this break-point current does not lie within the desired range of operation. At moderate current levels, where recombination effects are negligible, V_{ECO} is reduced by maintaining β_R (or β_F in the open-emitter case) as large as possible, as is clear from (3.8) and (3.9). The inevitable rise in external collector-emitter voltage at high currents, implicit in (3.10) and (3.11) is tamed somewhat by keeping the emitter series resistance to a minimum. In sum, with proper fabrication it should be possible to produce a ZBT having low, reasonably constant values of V_{ECO} over several decades of I_B.

Up until this point the effects of the parasitic substrate p-n-p's have been ignored. With recombination and high-current effects neglected, (1.5) and (1.10) enable the collector current to be written as

$$i_C = I_S\,(E\text{-}C) - \frac{I_S}{\beta_R}\,C - I_{SS}\,(C\text{-}S) \quad , \tag{3.25}$$

where

$$S = \exp\left(\frac{V_{SB}}{V_T}\right) \quad . \tag{3.26}$$

With the substrate reverse-biased S = 0; then for $i_C = 0$, (3.25) yields

$$V_{ECO} = V_T \ln\left(1 + \frac{1}{\beta_R} + \frac{I_{SS}}{I_S}\right) . \tag{3.27}$$

It can be seen that the substrate will substantially increase V_{ECO} if the ratio I_{SS}/I_S is comparable in magnitude to $1/\beta_R$. In the case of the Q009 device, for which $I_{SS}/I_S = 0.131$ and $1/\beta_R = 0.066$, (3.27) yields $V_{ECO} = 4.58$ mV. Without the parasitic p-n-p action (3.27) reduces to (3.8) and V_{ECO} is then only 1.63 mV. In these and all subsequent calculations T is taken to be 22.5°C. Parasitic action also results in a power drain due to I_{SUB}. For a symmetric device (1.6), (1.9) and (1.10) yield, under the conditions assumed in deriving (3.27),

$$\left|\frac{I_{SUB}}{I_E}\right|_{i_C=0} = \left(1 + \frac{1}{\beta}\frac{I_S}{I_{SS}}\right)^{-1} , \tag{3.28}$$

where $\beta = \beta_R = \beta_F$. For the Q009 device this ratio is calculated to be 0.663, an undesirable figure.

With reference to Figure 1.1, the parasitic effects can be reduced by extending the n^+ base contact diffusion down to the buried layer, thus suppressing the collection of holes at the junction between the n-type epitaxial layer and the p^{++} isolation wall. Incorporation of such a deep n^+ diffusion into conventional lateral p-n-p's has been found to reduce the open-collector ratio of I_{SUB} to I_E by a factor

ranging from over 4 at low currents to about 2 at I_E = 1mA [17].

It is useful to breifly consider a parallel configuration of two identical conventional asymmetric devices, with the two base terminals connected together, and the emitter terminal of one device connected to the collector terminal of the other and vice versa. Such a configuration might conceivably be employed in place of a single symmetric device. With the substrate, high-current, and recombination effects ignored, an analysis similar to that used to obtain (3.8) yields

$$V_{ECO} = V_T \ln \left[1 + \frac{1}{2}\left(\frac{1}{\beta_F} + \frac{1}{\beta_R}\right)\right] . \qquad (3.29)$$

Here one of the connected emitter-collector terminals has been arbitrarily defined as the emitter, and the other as the collector, with the latter left open. For the Q1 device, having parameters listed in Table 2.3, β_F = 50 and β_R = 1. Substitution of these values into (3.29) yields V_{ECO} = 10.5 mV. For a single symmetric device with $\beta_F = \beta_R$ = 50, (3.8) yields V_{ECO} = 0.501 mV. The parallel configuration is clearly inferior to the latter so far as dc performance is concerned.

3.2 Computer Simulation

The program SPICE, which employs the BJT model presented in Chapter One, was used to simulate the dc open-collector behaviour of the Q009 device. This simulation was performed both with and without the parasitic substrate devices, over a range of base currents of from 1nA to 10 mA. All parameters were taken from Tables 2.1 and 2.2. The

results are displayed in Figure 3.1, and clearly exhibit the features discussed in the preceding section.

Computer simulation was also carried out with the device operated with a fixed resistor connected in parallel with the collector and emitter terminals. Such resistors might be employed in cases where it is desirable to limit the maximum small-signal impedance between the collector and emitter terminals, for example in the feedback loop of an amplifier. As indicated by the results displayed in Figure 3.2, such parallel resistance substantially reduces the dc collector-emitter voltage at low base currents. This desirable consequence may be explained qualitatively by noting that a small current flows through the resistor into the collector terminal, which is at a negative voltage with respect to the emitter. This can only be due to an increase in the voltage V_{CB} across the forward-biased collector-base junction. Since V_{EC} is the difference $V_{EB} - V_{CB}$, it decreases. A quantitative account for this change using small-signal perturbation techniques is included in Chapter Four.

Open-collector and open-emitter simulations were also performed using the parameters listed for the conventional Q1 device. The relatively small recombination components of I_B caused V_{ECO} and V_{CEO} to remain close to the constant values predicted by (3.8) and (3.9), respectively, at moderate base currents.

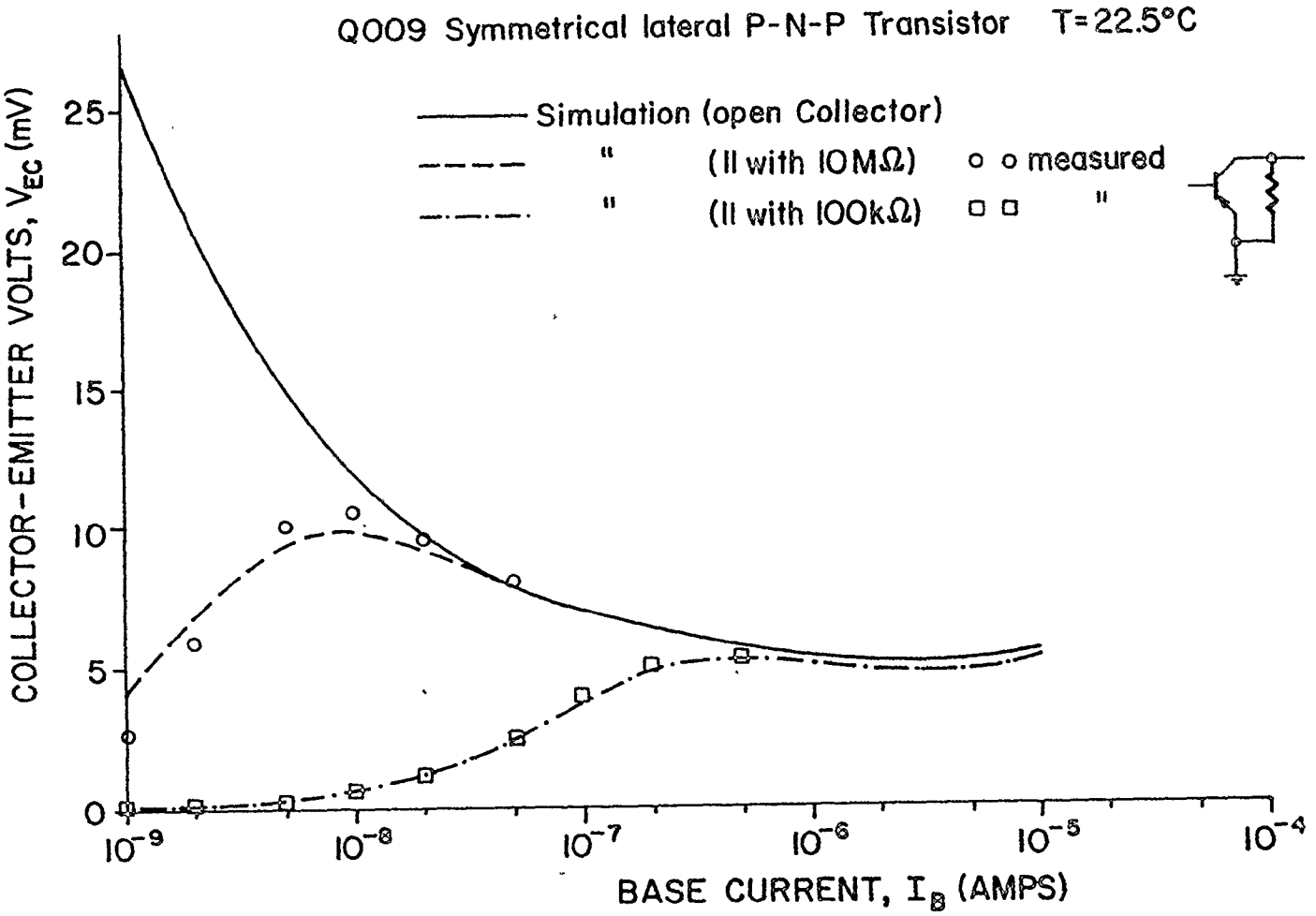

Figure 3.2. DC collector-emitter voltage of the Q009 device in parallel with a fixed resistance (substrate biased at -2V with respect to the emitter).

3.3 Experimental Results

The experimentally obtained V_{ECO} versus I_B data are shown in Figure 3.1. The base current was provided by the calibrated current source of a Tektronix Type 576 curve tracer; above 1 mA this was used in the pulsed mode. Below 1 mA V_{ECO} was measured with an electrometer (Keithley Type 610) having an input impedance of 10^{14} Ω. Above 1 mA V_{ECO} was displayed on the CRT of the curve tracer. The substrate was biased at -2V with respect to the grounded emitter. With the device inverted, a virtually identical set of measurements was obtained for V_{CEO}, as expected for a symmetric transistor.

It can be seen from Figure 3.1 that the measured and simulated results are in excellent agreement at low and moderate base currents. Above 100 μA the discrepancy noted in Chapter Two becomes apparent. Since precautions were taken to avoid errors caused by internal heating, this must be attributed to the onset of high-current effects not incorporated in the model. These include conductivity modulation in the active base region [13]. This can be important insofar as the voltage drop across the active base region can affect the V_{ECO} versus I_B characteristic at high base currents. Because of high power consumption and rising values of V_{ECO}, the ZBT is not likely to be used in this region in micropower applications. Figure 3.1 also illustrates the importance of modeling the substrate. When this is not done the simulated results are markedly inconsistent with the measurements in the mid-current region.

The results presented in Figure 3.1 establish the validity of

many of the expesssions derived in Section 3.1. The mid-current value of V_{ECO} predicted by (3.27), 4.58 mV, is in close agreement with the measured and simulated values. The values obtained by solving (3.23) account quite well for the rise in V_{ECO} at low base currents.

Measurements of V_{ECO} were also made with the Q009 transistor in parallel with 100 k Ω and 100 M Ω resistors. The results are presented in Figure 3.2. Once again, excellent corroboration is found between modeled and experimentally observed behaviour in the low and medium base current range.

CHAPTER 4

AC Characteristics of the Zero-Biased Transistor

This chapter is concerned with the modeling and understanding of the ac behaviour of the ZBT. Emphasis is placed on the small-signal collector-emitter device characteristics, including nonlinear distortion.

The Volterra-series approach is often employed in nonlinear small-signal analyses of the bipolar transistor [18], [19]. This consists of expanding each of the nonlinear elements of the large-signal model equations as a Taylor series, with the corresponding junction voltage as the independent variable. A perturbation method of analysis results in a set of complex linear node equations, one for each order. These are then solved separately and successively, beginning with the first order. Such a procedure is incorporated in the program SPICE, which computes solutions up to the third order.

4.1 Analytic Formulation

4.1.1 Small-Signal Device Characteristics

In the case of the ZBT it is possible to treat the device as a single nonlinearity at low frequencies by solving the large-signal model equations to obtain i_C in terms of I_B and v_{EC}. The result is then expanded as a Taylor series about the operating point $I_C = 0$, with v_{EC} as the independent variable and I_B as a parameter. This permits the

small-signal equations to be expressed in a tractable form.

From (3.6) and (1.5), for E, C >> 1,

$$i_C = \frac{I_S\ C}{q_b}\left(\frac{E}{C} - e_O\right) \quad . \tag{4.1}$$

With $I_C = 0$, i_C is then simply the small-signal current i_c. Similarly, $v_{EC} = V_{ECO} + v_{ec}$, where v_{ec} is the small-signal collector-emmiter voltage. Let x be defined by

$$x = v_{ec}/V_T \ ; \tag{4.2}$$

(4.1) now becomes

$$i_c = \frac{I_S\ C}{q_b}\, e_O\ (e^x - 1) \ . \tag{4.3}$$

It is useful to consider separately the small-signal behaviour at moderate levels of base current, where recombination is negligible, and at low levels, where recombination dominates. In both cases q_b is assumed to be unity, with the effects of high-level injection left to the section on computer simulation.

At moderate base currents (1.6) yields

$$i_B = I_B = \frac{I_S\ C}{\beta_R}\left(1 + \frac{1}{b}\, e_O\ e^x\right) , \tag{4.4}$$

with

$$b = \beta_F/\beta_R \ . \tag{4.5}$$

(4.3) and (4.4), with $q_b = 1$, are combined to yield i_c as a function of v_{ec} and I_B:

$$i_c = \frac{\beta_R \, I_B \, e_0}{1 + \frac{1}{b} e_0 \, e^x} (e^x - 1) \quad . \tag{4.6}$$

When the exponential terms in the numerator and demoninator are expanded as Taylor series about the point $v_{EC} = V_{ECO}$ (i.e. $I_C = 0$), and the mid-current expression (3.7) for e_0 utilized, (4.6) becomes

$$i_c = g_{eco} \left(v_{ec} + \frac{g_2}{g_{eco}} v_{ec}^2 + \frac{g_3}{g_{eco}} v_{ec}^3 \right) \quad , \tag{4.7}$$

where

$$g_{eco} = \frac{I_B}{V_T} \frac{\beta_F \, (\beta_R + 1)}{(\beta_F + \beta_R + 1)} \quad , \tag{4.8}$$

$$g_2/g_{eco} = \frac{1}{V_T} \left[\frac{1}{2} - \frac{\beta_R + 1}{\beta_R + \beta_F + 1} \right] , \tag{4.9}$$

and

$$g_3/g_{eco} = \frac{1}{V_T^2} \left[\frac{1}{6} - \frac{\beta_F \, (\beta_R + 1)}{(\beta_F + \beta_R + 1)^2} \right] . \tag{4.10}$$

The term g_{eco} is simply the small-signal collector-emitter conductance; the second and third-order nonlinearities in i_c are represented by g_2 and g_3, respectively. The ratios g_2/g_{eco} and g_3/g_{eco} are extremely useful in comparing the distortion-producing capabilities of two different devices for particular values of g_{eco}. Note that they are constant. Terms above the third order have been omitted; under small-signal conditions they will generally be negligible. For inverted operation, expansion of i_e yields expressions identical to (4.8) - (4.10) with β_R and β_F interchanged.

From (4.9) it is clear that second-order nonlinear distortion

vanishes for $\beta_F = \beta_R + 1$. In practice this condition is closely realized if $\beta_F \doteq \beta_R >> 1$. It is here that the advantages of a symmetric device become apparent. For conventional devices, where $\beta_F >> \beta_R$ and $\beta_F >> 1$, $|g_2/g_{eco}|$ approaches its maximum value of $1/2\ V_T$, which also holds true for g_2/g_{ceo} with the device inverted. The third-order term, given by (4.10), is found to vanish for $\beta_F = 3.72\ (\beta_R + 1)$. Under small-signal conditions third-order nonlinearities are generally of less concern than those of the second order; efforts are therefore primarily devoted to minimizing the latter. For a symmetric device with $\beta_F = \beta_R >> 1$, $g_3/g_{eco} \rightarrow 1/12\ V_T^2$, a factor of two lower than the value obtained when $\beta_F >> \beta_R$.

It is interesting to compare the small-signal behaviour of the bipolar transistor to that of an ideal diode. The current-voltage relationship for the latter is given by

$$i_D = I_S \left[\exp\left(\frac{v_D}{V_T}\right) - 1\right] , \qquad (4.11)$$

where i_D and v_D are the large-signal diode current and voltage respectively. Charge-storage effects have been neglected. With (4.11) expanded about the operating point $i_D = I_D$, the small-signal current i_d may be expressed as

$$i_d = \frac{I_D}{V_T}\left(v_d + \frac{v_d^2}{2V_T} + \frac{v_d^3}{6V_T^2}\right) . \qquad (4.12)$$

Terms above the third order have again been omitted. Comparison of the small-signal diode conductance I_D/V_T to that of a symmetric transistor

(for which $g_{eco} \rightarrow I_B \beta/2V_T$ when $\beta = \beta_F = \beta_R >> 1$) reveals that the dc current drawn by the latter is only about $1/\beta$ that required by the diode at a given conductance. Furthermore, the magnitudes of the nonlinear terms in (4.12) are only approached by the transistor under worst-case conditions (i.e. $\beta_F >> \beta_R$; $\beta_F >> 1$, or $\beta_R >> \beta_F$; $\beta_R >> 1$). Thus, the transistor would appear to be the obvious choice of the two devices for small-signal variable-impedance applications.

It is also interesting to compare the symmetric transistor to the parallel configuration of two identical conventional devices discussed in Chapter Three. An analysis of this configuration at moderate current levels yields

$$g_{eco} = \frac{2I_B}{V_T} \frac{\beta_F \beta_R (2\beta_F\beta_R + \beta_F + \beta_R)}{(\beta_F + \beta_R)(4\beta_F\beta_R + \beta_F + \beta_R)} \tag{4.13}$$

$$g_2/g_{eco} = \frac{1}{V_T} \left[\frac{1}{2} - \frac{2\beta_F\beta_R + \beta_F + \beta_R}{4\beta_F\beta_R + \beta_F + \beta_R}\right] \tag{4.14}$$

$$g_3/g_{eco} = \frac{1}{V_T^2} \left[\frac{1}{6} - \frac{2\beta_F\beta_R (2\beta_F\beta_R + \beta_F + \beta_R)}{(4\beta_F\beta_R + \beta_F + \beta_R)^2}\right] . \tag{4.15}$$

As a numerical example, let $\beta_F = 50$ and $\beta_R = 1$ (the parameters of the Q1 device listed in Table 2.3), with $T = 22.5^{\circ}C$. Then (4.14) and (4.15) yield, respectively, $g_2/g_{eco} = -3.99$ and $g_3/g_{eco} = -112$. For a symmetric device having $\beta_F = \beta_R = 50$, (4.9) and (4.10) yield, respectively, $g_2/g_{eco} = -0.194$ and $g_3/g_{eco} = -128$. While the third-order term g_3/g_{eco} is similar in each of the two cases, the parallel pair is seen to exhibit significantly greater second-order nonlinearity

than the comparable symmetric device. This is true in general when the reverse current gain β_R of each element of the parallel pair is close to unity and $\beta_F >> \beta_R$ (as is typically the case for conventional devices). Since second-order nonlinearities are usually of greater concern, the parallel-pair configuration has little to recommend it, especially in view of its inferior dc performance.

Plots of r_{eco} $(=1/g_{eco})$, g_2/g_{eco}, and g_3/g_{eco} for the Q009 device under moderate-current conditions are shown in Figures 4.1-4.3.

In the interest of analytic simplicity, the low-current small-signal behaviour of symmetric and conventional devices are considered separately. For the latter, the conditions $\beta_F >> \beta_R$ and $C_4 >> C_2$ (and $q_b = 1$) are assumed to hold. Then (3.13) and (4.3) yield

$$i_c = (I_S C + I_B)(e^x - 1) \cdot \tag{4.16}$$

From (3.14), derived for $n_C = 2$, C is seen to vary as a function of I_B only. Thus

$$i_c = I_B(\beta_R + 1)\left\{1 + \frac{I_{BL}}{2I_B}\left[1 - \left(1 + \frac{4I_B}{I_{BL}}\right)^{1/2}\right]\right\}(e^x - 1) \quad , \tag{4.17}$$

with I_{BL} defined by (3.15). With e^x expanded up to the third order, (4.17) can be expressed in a form identical to (4.7), with

$$g_{eco} = \frac{I_B(\beta_R + 1)}{V_T}\left\{1 + \frac{I_{BL}}{2I_B}\left[1 - \left(1 + \frac{4I_B}{I_{BL}}\right)^{1/2}\right]\right\} \quad , \tag{4.18}$$

$$g_2/g_{eco} = 1/2V_T \quad , \tag{4.19}$$

$$g_3/g_{eco} = 1/6V_T^2 \quad . \tag{4.20}$$

These expressions encompass both the low and moderate-current regions of operation. For $I_B >> I_{BL}$, (4.18) reduces to (4.8), when the condition $\beta_F >> \beta_R$ is applied to the latter. For $I_B << I_{BL}$, expansion of $(1 + 4I_B/I_{BL})^{1/2}$ in (4.18) gives

$$g_{eco} = \frac{I_B^2}{I_{BL}} \frac{(\beta_R + 1)}{V_T} \quad . \tag{4.21}$$

Thus g_{eco} varies from a linear function of I_B at moderate currents to a parabolic function of I_B at low currents.

With the device inverted, the expression for the resulting small-signal emitter-collector conductance g_{ceo} is identical to (4.18), except that the term $(\beta_R + 1)$ is replaced by β_R. The second and third-order terms are $-1/2V_T$ and $1/6V_T^2$, respectively.

In discussing the symmetric device, it is assumed that I_B is dominated by the recombination terms, and that $C_2 = C_4 = C_B$ and $n_C = n_E = n$. Recalling (3.20), C may then be expressed directly as a function of I_B and v_{EC}:

$$C = \left[\frac{I_S C_B}{I_B} \left(1 + e_o^{1/n} e^{x/n}\right)\right]^{-n} \quad . \tag{4.22}$$

Combination of (4.22) and (4.3), and expansion of the exponential terms in x as Taylor series about $v_{EC} = V_{ECO}$ enables i_c to be expressed in a form identical to (4.7), with

$$g_{eco} = \frac{I_B}{V_T} \frac{e_0}{(e_0 - 1)(1 + e_0^{1/n})} \tag{4.23}$$

$$g_2/g_{eco} = \frac{1}{V_T} \left[\frac{1}{2} - \frac{e_0^{1/n}}{1 + e_0^{1/n}}\right] \tag{4.24}$$

$$g_3/g_{eco} = \frac{1}{V_T^2} \left[\frac{1}{6} - \frac{1}{2} \left(\frac{n + 1}{n}\right)\left(\frac{e_0^{1/n}}{1 + e_0^{1/n}}\right)\right.$$

$$\left. + \frac{1}{2} \left(\frac{n + 1}{n}\right)\left(\frac{e_0^{1/n}}{1 + e_0^{1/n}}\right)^2\right] . \tag{4.25}$$

The expression (3.23) is used to solve for e_0. Plots of r_{eco} and g_2/g_{eco} under low-current conditions for the Q009 device are shown in Figures 4.1 and 4.2. In general g_2/g_{eco} rises slowly with decreasing base current, due to the increase in e_0 discussed in Chapter Three. The third-order term g_3/g_{eco} is positive at very low base currents, where the second and third terms in the bracketed quantity on the right-hand side of (4.25) tend to cancel. It is interesting to note that the mid-current value of g_3/g_{eco}, given by (4.10), is always negative for a symmetric device. Thus, a null in g_3/g_{eco} will be observed as I_B passes from the mid-current to the low-current region.

When $I_B \ll I_S C_B^2$ and $n = 2$, (4.25) reduces, with the aid of (3.24), to

$$g_{eco} \approx \frac{I_B^2}{I_S C_B^2} \frac{1}{V_T} . \tag{4.26}$$

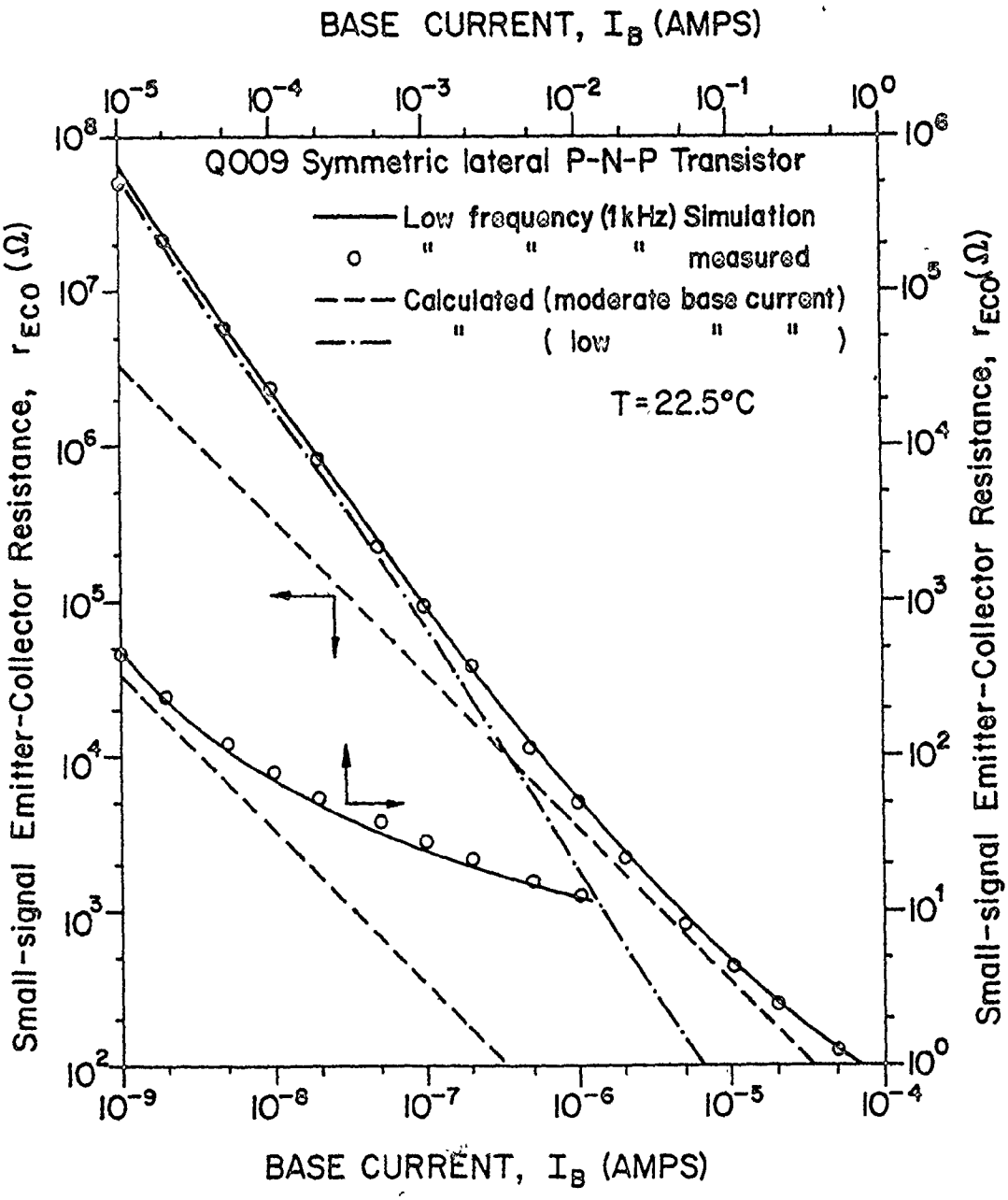

Figure 4.1. Small-signal collector-emitter resistance of the Q009 transistor as a function of base current.

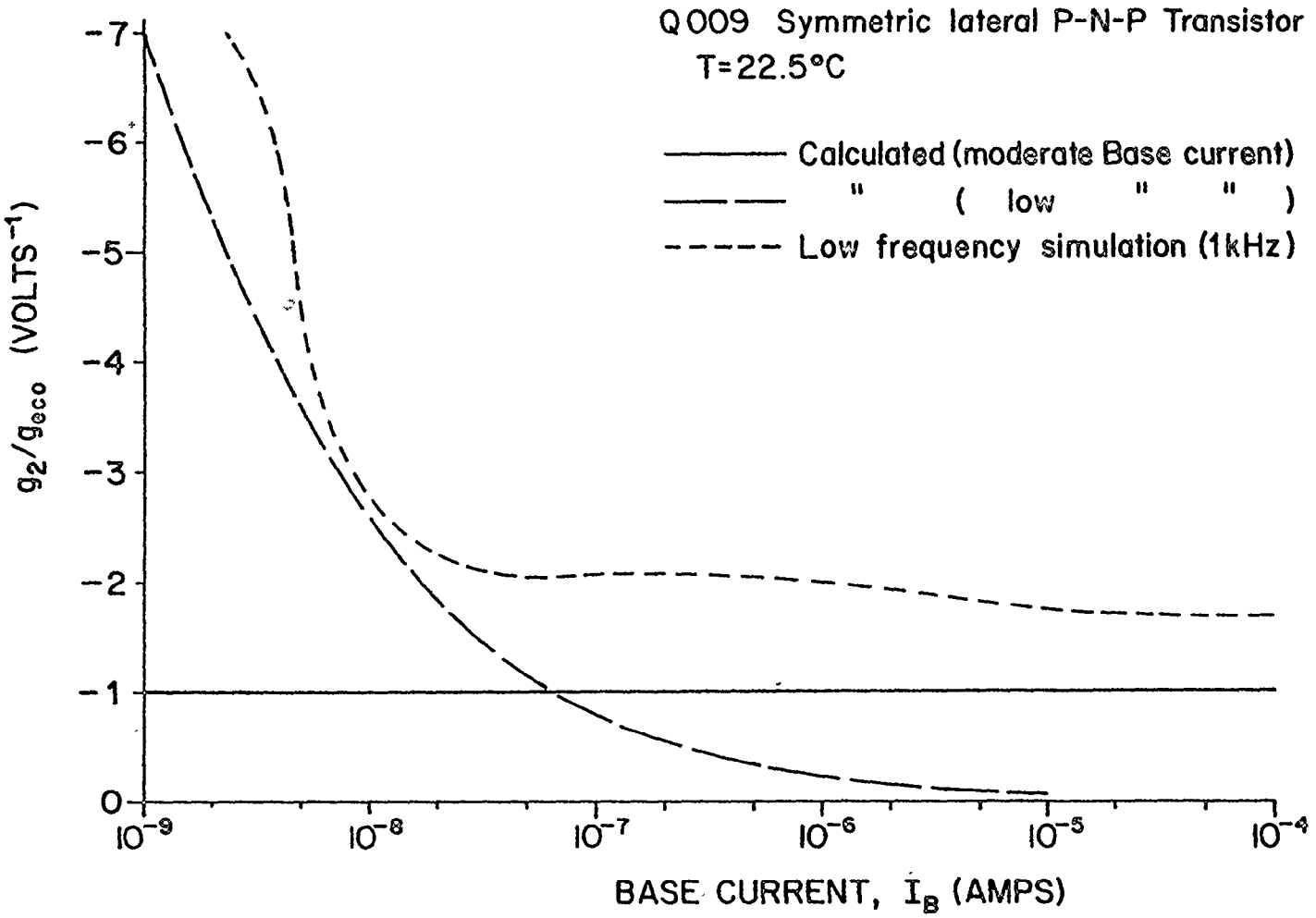

Figure 4.2. Second-order nonlinearity g_2/g_{eco} of the Q009 transistor as a function of base current.

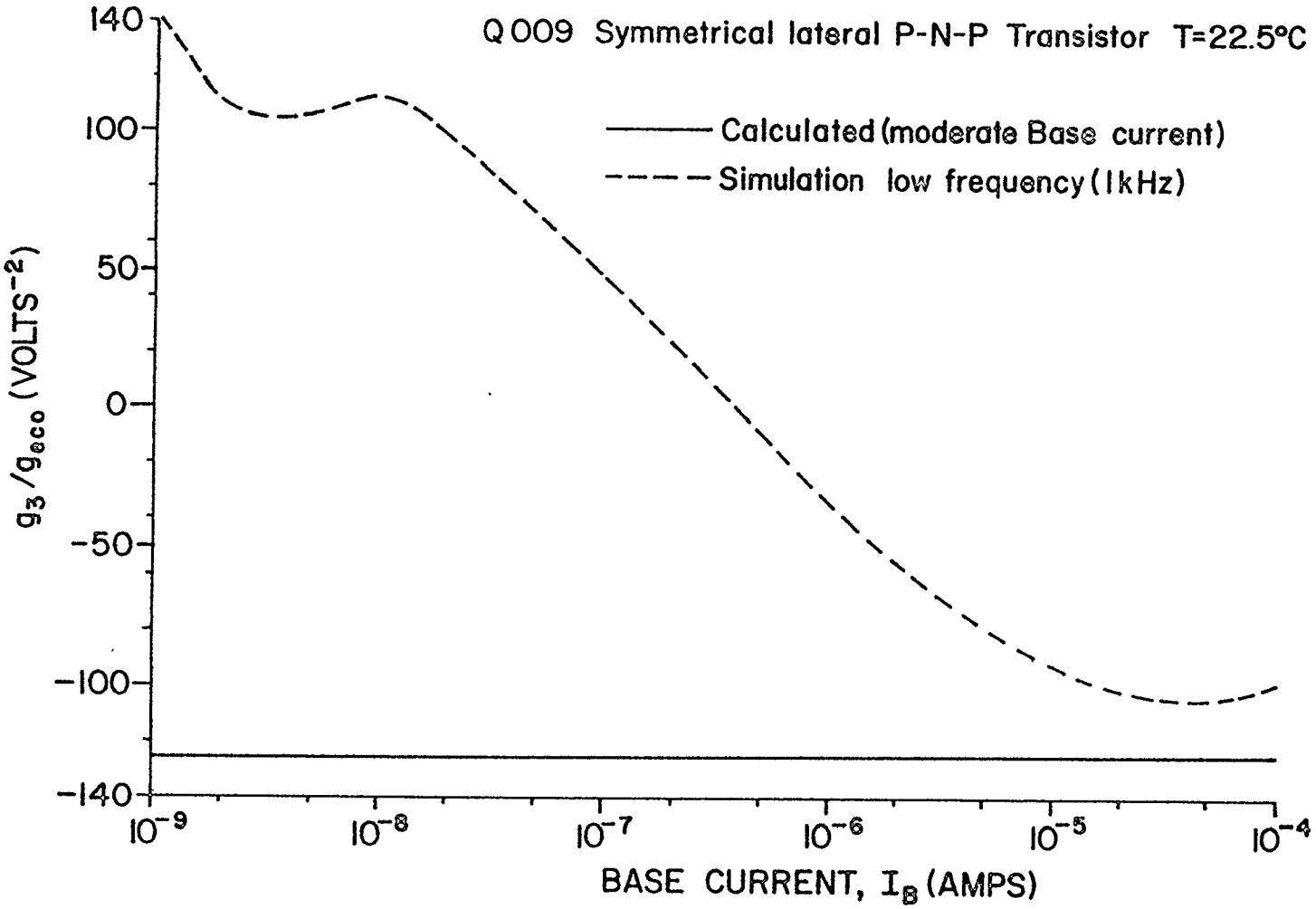

Figure 4.3. Third-order nonlinearity g_3/g_{eco} of the Q009 transistor as a function of base current.

This is very similar to the expression (4.21) obtained for the conventional device, with $I_{BL}/(\beta_R + 1)$ replaced by $I_S\ C_B^2$. Once again g_{eco} changes from a linear to a parabolic function at low currents. The break-point current marking this transition, $I_B = I_S\ C_B^2$, is identical to that at which V_{ECO} begins to rise. From a practical point of view this "corner" is undesirable, as it disrupts the linear relationship between the small-signal impedance and the controlling base current provided by (4.8). Thus the remarks made in Chapter Three about reducing recombination effects also apply here. Suppressing these effects also avoids the increase in g_2/g_{eco} and g_3/g_{eco} described above.

4.1.2 Effects of the Substrate

Thus far the effects of the substrate on the small-signal device behaviour have been neglected. They are most easily treated by first reverting to the Volterra-series approach discussed at the beginning of this chapter, in which each nonlinearity of the large-signal model equations is individually expanded as a Taylor series about the operating point. The first-order terms of the resulting small-signal model equations define the linear small-signal model, shown in Figure 4.4 for a three-terminal p-n-p device. The currents are defined to be positive when flowing out of the device.

In Figure 4.4,

$$g_f = \left.\frac{\partial\, i_C}{\partial\, v_{EB}}\right|_Q \qquad (4.27a)$$

$$g_r = \frac{\partial i_C}{\partial v_{CB}}\bigg|_Q \tag{4.27b}$$

$$g_\pi = \frac{\partial i_B}{\partial v_{EB}}\bigg|_Q \tag{4.27c}$$

$$g_\mu = \frac{\partial i_B}{\partial v_{CB}}\bigg|_Q . \tag{4.27d}$$

The low-frequency first-order model equations may then be written as

$$i_c = g_f v_{eb} + g_r v_{cb} \tag{4.28}$$

$$i_b = g_\pi v_{eb} + g_\mu v_{cb} . \tag{4.29}$$

First-order small-signal charge-storage effects are modeled by the capacitors c_π amd c_μ:

$$c_\pi = \frac{\partial q_E}{\partial v_{EB}}\bigg|_Q \tag{4.30a}$$

$$c_\mu = \frac{\partial q_C}{\partial v_{CB}}\bigg|_Q . \tag{4.30b}$$

The ohmic series resistances R_E, R_C, and R_B are added at the external terminals. They are omitted here, since their effect on the ZBT is assumed negligible outside the high-current region.

The higher-order terms of the nonlinear model equations can be represented as equivalent current sources added to the linear model of Figure 4.4 [18], [19]. These are used in solving the higher-order node

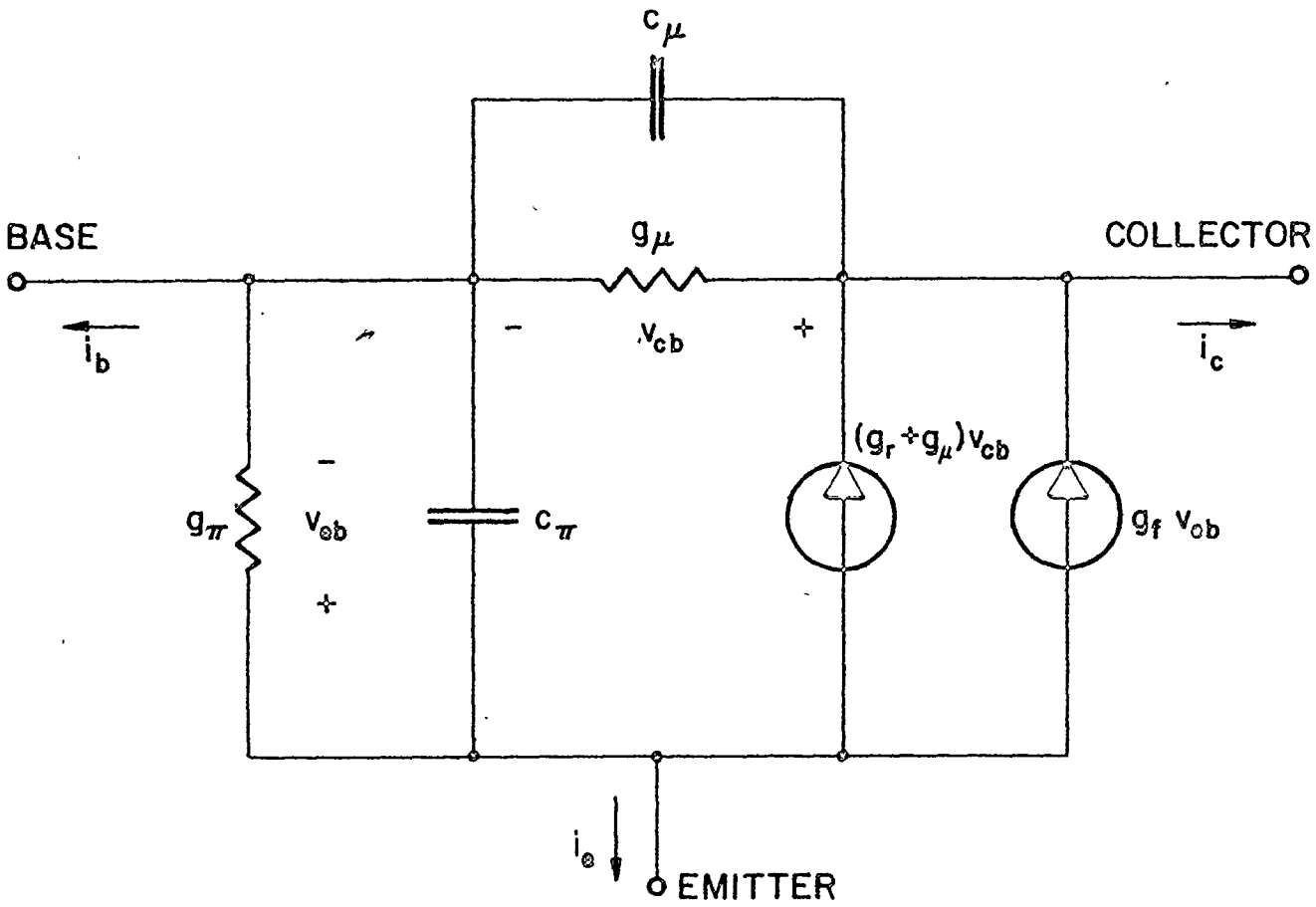

Figure 4.4. Linear small-signal model of the p-n-p transistor.

equations, following the perturbation method. In the case of the ZBT it is simpler at low frequencies to solve the first-order equations to obtain i_c in terms of v_{ec}, then expand the result as a power series in v_{ec} to include the higher-order terms. This reduces the number of equivalent current sources required at each order to one.

Before proceeding it is useful to obtain an expression for i_c in terms of the low-frequency first-order elements (4.7a)-(4.7d). With the assumption of an ideal current source supplying I_B, i_b is zero. Then (4.29) and Kirchhoff's laws enable v_{eb} and v_{cb} to be expressed in terms of v_{ec}:

$$v_{eb} = \frac{g_\mu}{g_\mu + g_\pi} v_{ec} \tag{4.31}$$

$$v_{cb} = \frac{-g_\pi}{g_\mu + g_\pi} v_{ec} \quad . \tag{4.32}$$

This enables (4.28) to be expressed as

$$i_c = \left(\frac{g_f - g_r\, g_\pi/g_\mu}{1 + g_\pi/g_\mu}\right) v_{ec} \quad . \tag{4.33}$$

With the right-hand side expanded as a Taylor series with v_{ec} as the independent variable, (4.33) may be expressed in a form identical to (4.8), with

$$g_{eco} = f\{v_{eb}, v_{cb}\} \Big|_{I_C = 0} \tag{4.34}$$

$$g_2 = \frac{1}{2} \frac{d}{d\, v_{ec}} f\{v_{eb}, v_{cb}\} \Big|_{I_C = 0} \quad . \tag{4.35}$$

$$g_3 = \frac{1}{6} \frac{d^2}{d\, v_{ec}^2} f\{v_{eb}, v_{cb}\} \Big|_{I_C = 0} , \tag{4.36}$$

where

$$f\{v_{eb}, v_{cb}\} = \frac{g_f - g_r \beta_\pi / g_\mu}{1 + g_\pi / g_\mu} . \tag{4.37}$$

Assume recombination and high-current effects to be negligible. Then from (1.5) and (1.6), the low-frequency first-order elements are

$$g_f = \frac{I_S\, E}{V_T} \tag{4.38a}$$

$$g_r = -\left(1 + \frac{1}{\beta_R}\right) \frac{I_S\, C}{V_T} \tag{4.38b}$$

$$g_\pi = \frac{1}{\beta_F} \frac{I_S\, E}{V_T} \tag{4.38c}$$

$$g_\mu = \frac{1}{\beta_R} \frac{I_S\, C}{V_T} . \tag{4.38d}$$

Substitution of (4.38a)-(4.38d) into (4.34) yields, with the aid of (3.7),

$$g_{eco} = g_{fo} , \tag{4.39}$$

where g_{fo} is the value of g_f at $I_C = 0$. Note that g_{fo} is simply the quantity on the right-hand side of (4.8).

The parasitic substrate devices are readily incorporated into the nonlinear small-signal model. Under the assumptions stated in the preceding paragraph, and with the substrate reverse-biased, (1.5), (1.6), (1.9), (1.10) and Figure 1.3 enable i_C, i_B and i_E to be written

as

$$i_C = I_S\ (E - C) - \frac{I_S}{\beta_R} C - I_{SS}\ C \tag{4.40}$$

$$i_B = \frac{I_S}{\beta_F} + \frac{I_S}{\beta_R} \tag{4.41}$$

$$i_E = - I_S\ (E - C) - \frac{I_S}{\beta_F} E - I_{SS}\ E \quad . \tag{4.42}$$

Inspection of (4.40) and (4.42) reveals that two new elements must now be included in the first-order small-signal model, in addition to those given by (4.38a)-4.38d). These are defined by

$$g_{sr} = \left. \frac{\partial\ i_C}{\partial\ v_{CB}} \right|_Q \tag{4.43a}$$

$$g_{sf} = \left. \frac{\partial\ i_E}{\partial\ v_{EB}} \right|_Q \quad . \tag{4.43b}$$

Then from (4.40) and (4.42),

$$g_{sr} = - \frac{I_{SS}\ C}{V_T} \tag{4.44a}$$

$$g_{sf} = - \frac{I_{SS}\ E}{V_T} \quad . \tag{4.44b}$$

The first-order expressions for i_c and i_e may then be written as

$$i_c = g_f\, v_{eb} + g_r\, v_{cb} + g_{sr}\, v_{cb} \tag{4.45}$$

$$i_e = -\, g_f\, v_{eb} - g_r\, v_{cb} - g_\pi\, v_{eb} - g_\mu\, v_{eb} + g_{sf}\, v_{eb} \quad . \tag{4.46}$$

At high frequencies the capacitor c_{SUB}, defined by

$$c_{SUB} = \frac{\partial\, q_{SUB}}{\partial\, v_{SB}} \Bigg|_Q \quad , \tag{4.47}$$

is added across the base-substrate junction. The linear small-signal p-n-p model with the parasitic substrate devices included is shown in Figure 4.5.

If the base current supply is assumed to be ideal, the expressions (4.31) and (4.32) are found to hold true even with the parasitic substrate devices included in the model. This enables (4.45) to be expressed as

$$i_c = \left[\frac{g_f - g_r\, g_\pi/g_\mu}{1 + g_\pi/g_\mu} - g_{sr}\left(\frac{g_\pi/g_\mu}{1 + g_\pi/g_\mu}\right)\right] v_{ec} \quad . \tag{4.48}$$

When $I_C = 0$ the bracketed term is equal to g_{eco}. Using (4.48), (4.38a)-(4.38d) and (4.44a), one obtains, with the aid of (3.27) and (4.41),

$$g_{eco} = \frac{I_B}{V_T}\left[\frac{\beta_F\,(\beta_R + 1) + \beta_F \beta_R (I_{SS}/I_S)}{\beta_F + \beta_R + 1 + \beta_R (I_{SS}/I_S)}\right] \quad . \tag{4.49}$$

Note that for $I_{SS} = 0$ (4.49) reduces to (4.8). The influence of the parasitic substrate transistors on g_{eco} is small for $I_{SS}/I_S \ll 1$. In the case of the Q009 device, for which $I_{SS}/I_S = 0.131$, the values of

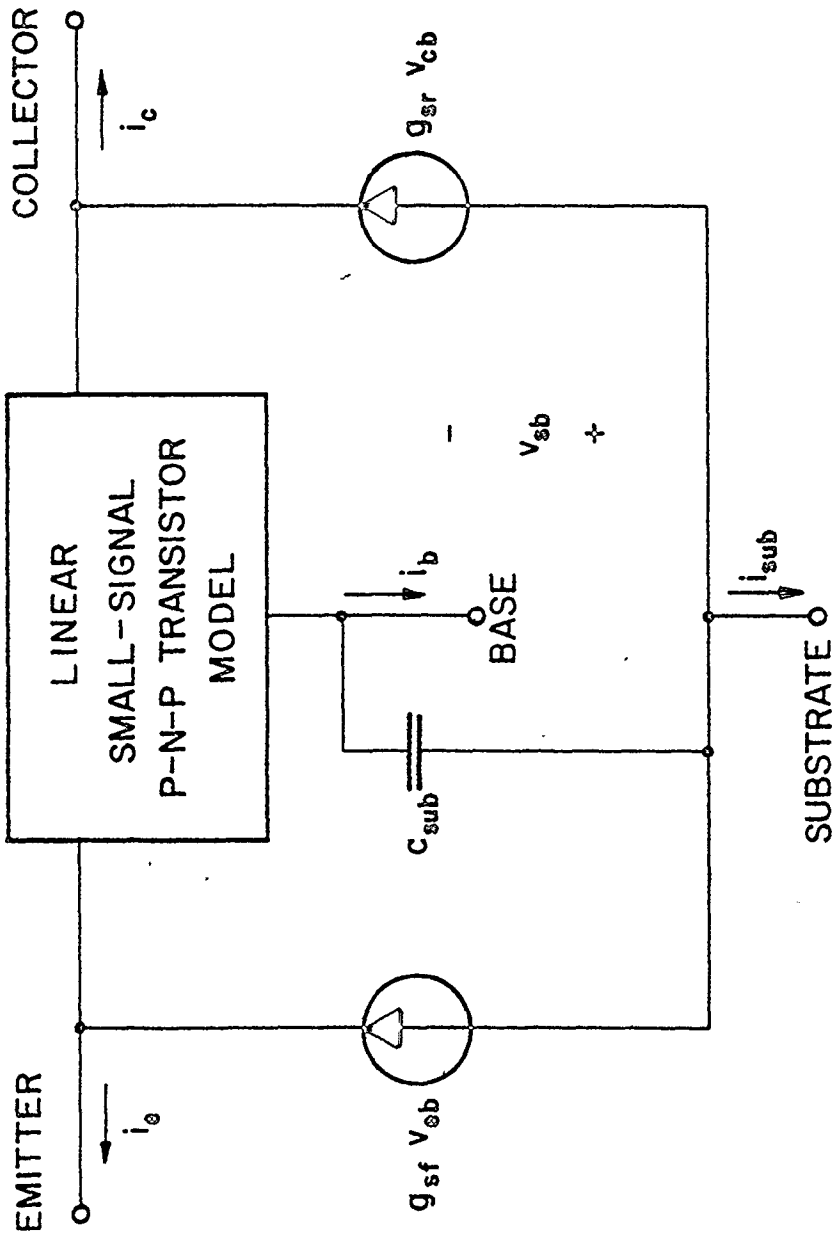

Figure 4.5. Linear small-signal model of the p-n-p transistor including the substrate, with the substrate reverse-biased.

g_{eco} obtained using (4.49) differ by 5% at any given base current from the values of g_{eco} calculated using (4.8). Contrast this with the dramatic effect of the substrate on V_{ECO} at moderate base currents for the Q009 device, discussed in Chapter Three.

The higher-order terms of i_c are obtained by expanding (4.48). The effects of the parasitic substrate transistors on device nonlinearity are more readily determined by means of computer simulation. This is discussed in Section 4.2.

4.1.3 Effects of a Parallel Resistance

As was stated in the preceding chapter, the ZBT is likely in many applications to be employed in parallel with a fixed resistance between the collector and emitter terminals. The dc collector current is no longer zero in this case; if R_p is the fixed resistance, then

$$\begin{aligned} i_C &= V_{EC}/R_p \\ &= V_{EC}\, G_p \quad , \end{aligned} \tag{4.50}$$

where $G_p = 1/R_p$. Under small-signal conditions, i_c can be expressed in the form of (4.7), which is repeated here for reference:

$$i_c = g_{eco}\, v_{ec} + g_2\, v_{ec}^2 + g_3\, v_{ec}^3 \quad , \tag{4.51}$$

with $v_{ec} = v_{EC} - V_{ECO}$. Assume that i_C is sufficiently small that it can be treated as a small-signal perturbation. Then if Kirchhoff's law is applied at the collector terminal, (4.50) and (4.51), with the higher order terms neglected, yield

$$V_{EC} = \frac{1}{1 + G_p/g_{eco}} V_{ECO} \quad . \tag{4.52}$$

With g_{eco} obtained using (4.8) or (4.23) (depending on the base current level), the deviation in V_{EC} from its open-collector value due to G_p is readily obtained with the aid of (4.52). When this is done for the Q009 device, with values of V_{ECO} taken from the measured points of Figure 3.1, the resulting V_{EC} versus I_B characteristics for $R_p = 10^5$ Ω and $R_p = 10^7$ Ω are found to be in very close agreement with the measured characteristics of Figure 3.2.

Assuming once again that i_c can be treated as a small-signal perturbation, the change in small-signal collector-emitter conductance due to G_p may be estimated. Let this change be defined as Δg_{ec}. Then, using (4.51),

$$\Delta g_{ec} \simeq \left. \frac{\partial g_{ec}}{\partial v_{ec}} \right|_{I_C = 0} \cdot (V_{EC} - V_{ECO})$$

$$= 2 g_2 (V_{EC} - V_{ECO}) \quad . \tag{4.53}$$

Then with the aid of (4.52)

$$\frac{\Delta g_{ec}}{g_{eco}} \simeq - 2 \left(\frac{g_2}{g_{eco}}\right) \frac{V_{ECO}}{1 + g_{eco}/G_p} \quad . \tag{4.54}$$

In general this change will be quite small. In the case of the Q009 device, with $G_p = 10^{-5}$ mhos, $\Delta g_{ec}/g_{eco}$ is found, using (4.8), (4.9) and (4.54), to be 2.5×10^{-3} when $I_B = 10^{-8}$ A, decreasing to 1.1×10^{-5} when $I_B = 10^{-5}$ A. A similar type of analysis can be used to show that the changes in the higher-order terms g_2 and g_3 due to the parallel

resistance R_p are also very small, and can generally be neglected.

With reference to (4.6), the small signal expansion for i_c is valid only for $|x| << x^2/2$; that is, $|v_{EC} - V_{ECO}| << 2\ V_T$. Then from (4.51) and (4.52) the small-signal approximation for the collector current is valid only for

$$\frac{R_p}{r_{eco}} + 1 >> \frac{V_{ECO}}{2\ V_T} \quad . \tag{4.55}$$

In practice this condition will always hold, except possibly at very low base currents, when r_{eco} is very large and V_{ECO} may exceed $2\ V_T$.

4.1.4 Effects of a Finite Base-Drive Impedance

Under real operating conditions the current source supplying the base current of the ZBT has a finite output impedance R_S. The equivalent small-signal representation of this current source is simply a conductance G_S between the base and emitter terminals. Then with reference to Figure 4.1, (4.28), and (4.29), the resulting circuit equations are

$$i_c = g_f\ v_{eb} + g_r\ v_{cb} \tag{4.55a}$$

$$G_S\ v_{eb} + g_\pi\ v_{eb} + g_\mu\ v_{cb} = 0. \tag{4.55b}$$

Solution for i_c in terms of v_{ec} yields

$$i_c = \left[\frac{g_f g_\mu - g_r g_\mu - g_r\ G_S}{g_\mu + g_\pi + G_S}\right] v_{eco} \quad . \tag{4.56}$$

Evaluation of the bracketed quantity for $I_C = 0$ yields, with the aid of (3.7) and (4.38a)-(4.38d),

$$g_{eco} = g_{fo} \quad . \tag{4.57}$$

This is identical to (4.39), the result obtained under the assumption of an ideal base current source. Expanding (4.56) in terms of v_{ec}, one obtains, again with the aid of (3.7) and (4.38a)-(4.38d),

$$g_2/g_{eco} = \frac{1}{\left(1 + \frac{G_S V_T}{I_B}\right)} \frac{1}{2 V_T} \left[\frac{1}{2} - \frac{\beta_R + 1}{\beta_R + \beta_F + 1}\right]$$

$$- \frac{1}{2 V_T} \left(\frac{G_S}{g_{eco}}\right) \frac{\frac{g_{eco} V_T}{I_B} \left[A^2 \left(1 + \frac{G_S V_T}{I_B}\right) - 1\right] - (\beta_R + 1)}{A^2 \left(1 + \frac{G_S V_T}{I_B}\right)^2} \quad , \tag{4.58}$$

where

$$A = \frac{\beta_F + \beta_R + 1}{\beta_F} \quad . \tag{4.59}$$

Note that as $G_S \to 0$ (4.58) reduces to (4.9).

It is apparent from (4.58) that the effect of G_S on second-order nonlinear distortion is negligible under the condition

$$\frac{G_S V_T}{I_B} \ll 1. \tag{4.60}$$

When this condition is violated $\left| g_2/g_{eco} \right|$ increases dramatically, approaching $1/(2V_T)$ as $R_S \to 0$. Similarly, third-order nonlinear distortion rises as R_S decreases.

4.1.5 ZBT Attenuator Circuit

Figure 4.6 shows a simple small-signal attenuator circuit employing the ZBT. The blocking capacitor C_B will not affect performance above 50 Hz, even with r_{eco} as low as 10 Ω. The output terminal is shown unloaded; loads of finite impedance will appear in parallel with R_p. Note that R_p has been connected directly across the transistor. As discussed in Section 4.1.3, the small-signal expressions developed for $I_C = 0$ will continue to be valid. Furthermore, direct connection of R_L to the transistor has the beneficial effect of suppressing the rise in V_{ECO} at low base currents.

With the output assumed to be unloaded, the nonlinear small-signal circuit equation can be written

$$G_L (v_i - v_o) - G_p v_o - i_c = 0 \quad , \tag{4.61}$$

where i_c is the nonlinear small-signal collector current. At low frequencies i_c can be written as an expansion in the form of (4.51), with v_{ec} as the independent variable. Noting that $v_o = v_{ec}$, (4.61) becomes

$$G_L (v_i - v_o) - G_p v_o - g_{eco} v_o - g_2 v_o^2 - g_3 v_o^3 = 0 \quad . \tag{4.62}$$

At high frequencies the expansion for i_c will include time-dependent terms which are due to the nonlinear charge-storage elements q_E and q_C.

Assume that the small-signal output voltage v_o may be written as

$$v_o(t) = \sum_{m=1}^{3} H_m v_i^m(t) \quad , \tag{4.63a}$$

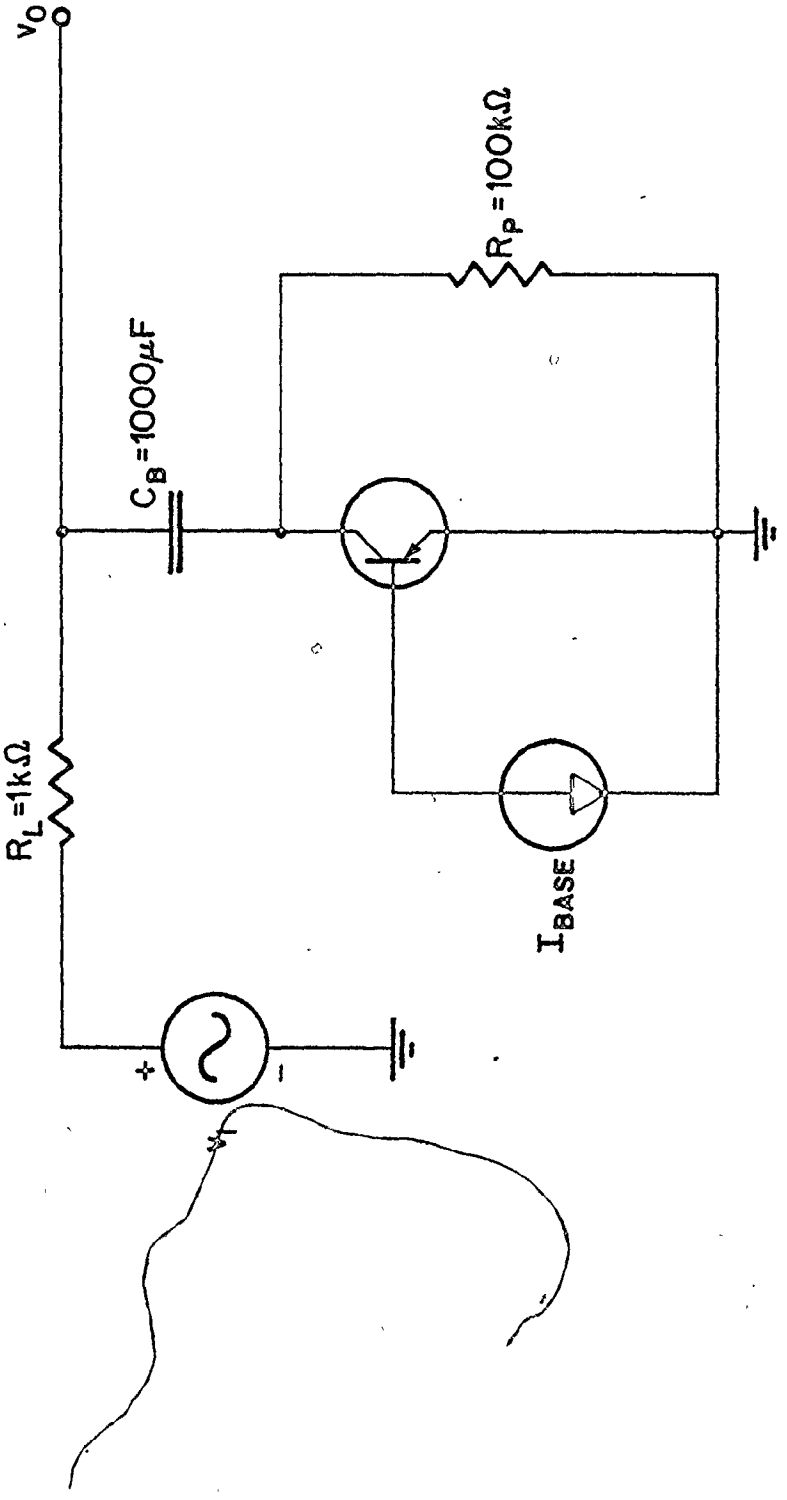

Figure 4.6. ZBT small-signal attenuator circuit.

with $$\left| H_1 \, v_i(t) \right| >> \left| H_2 \, v_i^2(t) \right| >> \left| H_3 \, v_i^3(t) \right| \quad . \tag{4.63b}$$

H_1, H_2, and H_3 are, respectively, the first, second, and third-order transfer functions of the circuit. Substitution of (4.63a) into (4.62) yields

$$\begin{aligned} & v_i(t) \, [G_L \, (1 - H_1) - (G_p + g_{eco}) \, H_1] \\ & + v_i^2(t) \, [-G_L \, H_2 - (G_p + g_{eco}) \, H_2 - g_2 \, H_1^2] \\ & + v_i^3(t) \, [-G_L \, H_3 - (G_p + g_{eco}) \, H_3 - 2 \, g_2 \, H_1 \, H_2 \\ & - g_3 \, H_1^3] = 0 \quad . \end{aligned} \tag{4.64}$$

Terms above the third order have been omitted. Following the perturbation method [18], [20], the second and third-order terms are neglected and the first-order term solved for H_1. This yields

$$H_1 = \frac{G_L}{g_{eco} + G_p + G_L} \quad . \tag{4.65a}$$

Note that H_1 is simply the linear transfer function of the circuit. Similarly, with the third-order term neglected, (4.64) is solved for H_2. This yields

$$H_2 = \frac{- g_2 \, H_1^2}{g_{eco} + G_p + G_L} \quad . \tag{4.65b}$$

Finally, solution for H_3 yields

$$H_3 = \frac{-2 \, g_2 \, H_1 \, H_2 - g_3 \, H_1^3}{g_{eco} + G_p + G_L} \quad . \tag{4.65c}$$

Consider an input signal of the form

$$v_i(t) = v_i \cos \omega t \quad , \tag{4.66a}$$

where v_i is a constant. Then

$$v_i^2(t) = \frac{v_i^2}{2} \ (\cos 2\omega t + 1) \tag{4.66b}$$

$$v_i^3(t) = \frac{v_i^3}{4} \ (\cos 3\omega t + 3 \cos \omega t) \ . \tag{4.66c}$$

With reference to (4.63a), the dc term of $v_i^2(t)$ appears in $v_o(t)$, and can cause a small change in the dc operating point of the ZBT. However, when the condition (4.63b) is satisfied its effect is negligible. Similarly, $v_i^3(t)$ gives rise to a term $\frac{3}{4} H_3 v_i^3 \cos \omega t$ appearing in $v_o(t)$. This adds to the term $H_1 v_i \cos \omega t$, giving rise to expansion or compression of the fundamental frequency component of $v_o(t)$. This too is negligible when (4.63b) is satisfied. Then (4.63a) may be written as

$$v_o(t) = H_1 v_i \cos \omega t + \frac{1}{2} H_2 v_i^2 \cos 2\omega t + \frac{1}{4} H_3 v_i^3 \cos 3\omega t \ . \tag{4.67}$$

Define the fractional second harmonic distortion HD_2 as the ratio of the amplitude of the second harmonic at the output to the amplitude to the fundamental at the output. Then from (4.67)

$$HD_2 = \frac{1}{2} \frac{H_2}{H_1} v_i \tag{4.68a}$$

Similarly, define the fractional third harmonic distortion HD_3 as the ratio of the amplitude of the third harmonic at the output to the fundamental at the output. From (4.67)

$$HD_3 = \frac{1}{4} \frac{H_3}{H_1} v_i^2 \quad . \tag{4.68b}$$

These quantities are readily evaluated for the attenuator circuit using (4.65a)-(4.65c):

$$HD_2 = - \frac{1}{2} \frac{g_2 H_1^2}{G_L} v_i \tag{4.69a}$$

$$HD_3 = \frac{1}{4} \frac{H_1^3}{G_L} \left[\frac{2 g_2^2 H_1}{G_L} - g_3 \right] v_i^2 \quad . \tag{4.69b}$$

It is apparent from (4.65a) that H_1 approaches unity for $g_{eco} << G_p$. Since g_2 and g_3 decrease with g_{eco}, second and third harmonic distortions are minimized for $H_1 \to 1$.

Intermodulation distortion, which is usually of greater consequence in practical applications, is readily analyzed by considering an input signal of the form

$$v_i(t) = A_1 \cos \omega_1 t + A_2 \cos \omega_2 t \ . \tag{4.70}$$

This is substituted into (4.63a) to obtain the second and third-order intermodulation terms of $v_o(t)$. Under small-signal conditions these are found to be constant multiples of the corresponding harmonic distortion terms [20].

4.1.6 Variable-Gain Feedback Amplifier

The techniques used in the preceding section can be applied to circuits of arbitrary complexity. As an illustration, consider the circuit of Figure 4.7, where the ZBT is employed in the feedback loop of an amplifier. The gain thus depends on g_{eco}, which is controlled by I_B. If the open-loop gain of the amplifier is very large, $v_f \approx v_i$, and Kirchhoff's law yields simply

$$G_1 v_i = i_c$$

$$= g_{eco} (v_o - v_i) + g_2 (v_o - v_i)^2$$

$$+ g_3 (v_o - v_i)^3 \quad . \tag{4.71}$$

When v_o is expressed in the form of (4.63a), the first-order circuit equation becomes

$$G_1 v_i = -g_{eco} (H_1 - 1) v_i \quad , \tag{4.72}$$

which yields

$$H_1 = 1 + G_1/g_{eco} \quad .$$

This is simply the small-signal gain of the amplifier. The second-order equation is

$$g_{eco} H_2 + g_2 (H_1^2 - 2H_1 + 1) = 0 \quad , \tag{4.73}$$

which when solved for H_2 yields

$$H_2 = -\frac{g_2}{g_{eco}} (H_1 - 1)^2 \quad . \tag{4.74}$$

Similarly, solution of the third-order circuit equation yields

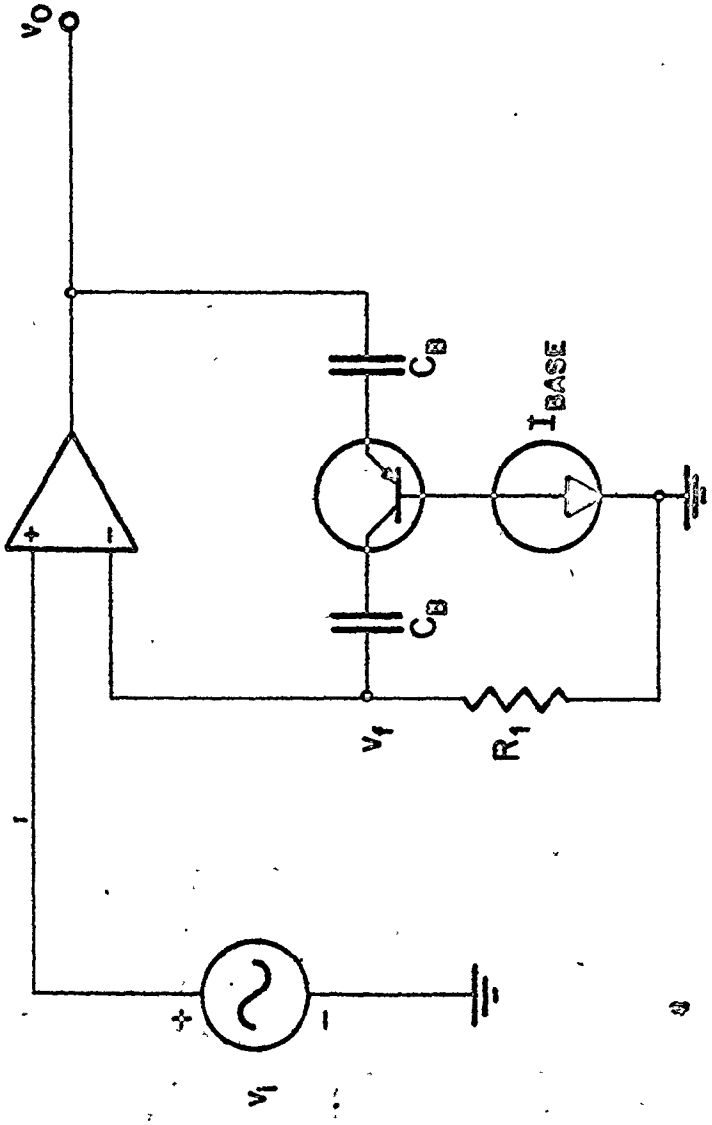

Figure 4.7. Variable-gain feedback amplifier employing the ZBT.

$$H_3 = \frac{1}{G_1 + g_{eco}} \left[2g_2 H_2 (H_1 - 1) - g_3 (H_1 - 1)^3\right] \quad . \qquad (4.74)$$

The fractional second harmonic distortion, as defined by (4.68a) is

$$HD_2 = -\frac{1}{2} \frac{g_2}{g_{eco}} \frac{(H_1 - 1)^2}{H_1} \; v_i \quad , \qquad (4.76)$$

which for $H_1 >> 1$ reduces to

$$HD_2 = -\frac{1}{2} \frac{g_2}{g_{eco}} \; H_1 \; v_i \quad . \qquad (4.77)$$

As expected, the second harmonic distortion rises when the gain of the amplifier is increased.

4.2 Computer Simulation

The program SPICE [4] [5], which employs the BJT model discussed in the first chapter, was used to simulate the ac behaviour of the Q009 device. The input parameters used are those listed in Table 2.1; the device operating temperature was taken to be 22.5°C. Simulation was performed both with and without the parasitic substrate devices; the parameters of the latter are listed in Table 2.2.

The small-signal resistance r_{eco} was obtained with the device operated in parallel with a 10^{12} Ω resistor between the collector and the grounded emitter, with an ideal ac voltage source coupled to the collector terminal through a large blocking capacitor. This is in essence an open-collector configuration. The results obtained at a frequency of 1 kHz, with the substrate biased at -2V with respect to the

emitter, are shown in Figure 4.1. At low base currents r_{eco} approaches the asymptote predicted by (4.23). As I_B is increased, r_{eco} begins to approach the asymptote predicted by (4.8). At very high base currents the high-level injection term q_b becomes important, and r_{eco} deviates from this line. Eventually r_{eco} approaches the constant value $R_E + R_C$, which is 8 Ω in the case of the Q009 device.

With the substrate omitted the simulated values of r_{eco} were found to be about 5% higher than those shown in Figure 4.1, as was calculated in Section 4.1.2. With the device operated in parallel with fixed resistances of 100 k Ω and 10 M Ω, the simulated small-signal collector-emitter resistance of the device remained virtually unchanged from its open-collector value r_{eco}, supporting the conclusion reached in Section 4.1.3.

High-frequency effects, which are difficult to analyze through manual computation, are easily simulated with the aid of a computer. The small-signal resistance r_{eco} was found to remain constant for the Q009 device up to a frequency of 5 MHz, above which point it decreased, asymptotically approaching a slope of 6dB/octave. When both the emitter-base and collector-base junctions are forward-biased, as is the case with the ZBT, this decrease is due chiefly to the small-signal capacitance associated with the diffusion component of the stored charge, modeled by τ_F and τ_R.

The small-signal nonlinear device behaviour was simulated with the ZBT incorporated into the attenuator circuit of Figure 4.6. Again the substrate was biased at -2V. Simulation was carried out at

frequencies of 1 kHz and 10 kHz. The fractional second and third-harmonic distortions for a constant output signal of 10 mV rms at the fundamental frequency are plotted in Figures 4.8 and 4.9, respectively. Note the marked increase in HD_2 at 10 kHz, especially at low base currents. This is due to the second-order nonlinearities associated with the charge-storage terms q_E and q_C. The program SPICE lists the contributions of each element of the BJT model to the total harmonic distortion. The contributions of q_E and q_C to HD_2 are negligible at 1 kHz, but become significant at 10 kHz. Third harmonic distortion remains virtually unchanged at 10 kHz. Note also the null in HD_3 at $I_B = 6 \times 10^{-7}$ A. This is due to the null in g_3, discussed earlier, which occurs during the transition from the low base current to the moderate base current region of operation.

With the aid of (4.65a)-(4.65d), g_2/g_{eco} and g_3/g_{eco} were calculated from the low-frequency (1 kHz) values of HD_2 and HD_3. They are shown in Figures 4.2 and 4.3. As base current is reduced, g_2/g_{eco} increases, closely following the curve predicted by (4.25). At moderate base currents g_2/g_{eco} is virtually independent of I_B. Note that the value of g_2/g_{eco} in this region is approximately twice that calculated using (4.9). This is due to the parasitic substrate transistors; when these are removed, the simulated value of g_2/g_{eco} decreases by a factor of two at moderate base currents. With reference to Figure 4.3, it can be seen that g_3/g_{eco} is strongly influenced by the recombination terms of the model equations, even at relatively high base currents. Only when $I_B > 10$ μA does g_3/g_{eco} approach the mid-current value predicted by

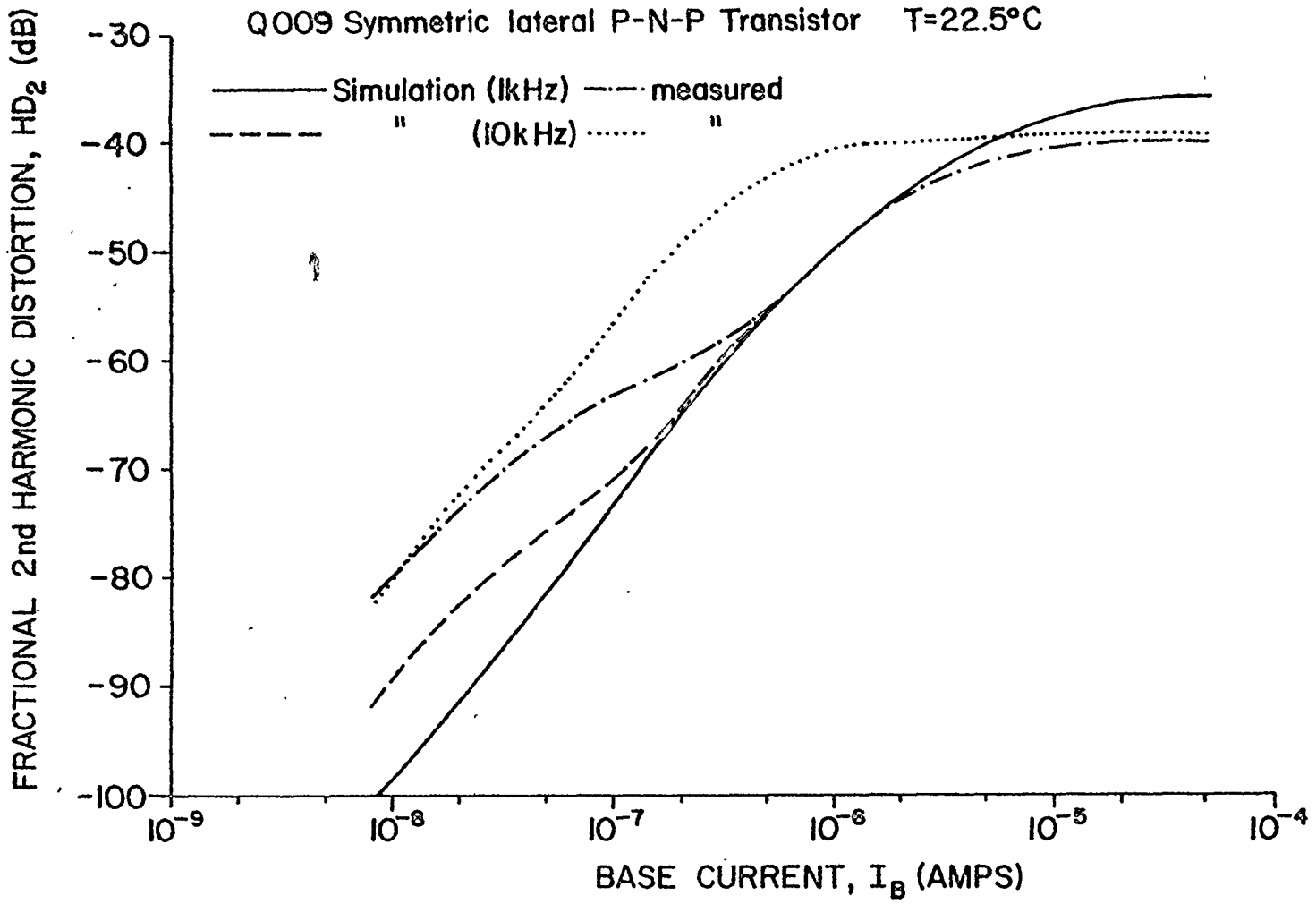

Figure 4.8. Fractional second harmonic distortion of the ZBT small-signal attenuator.

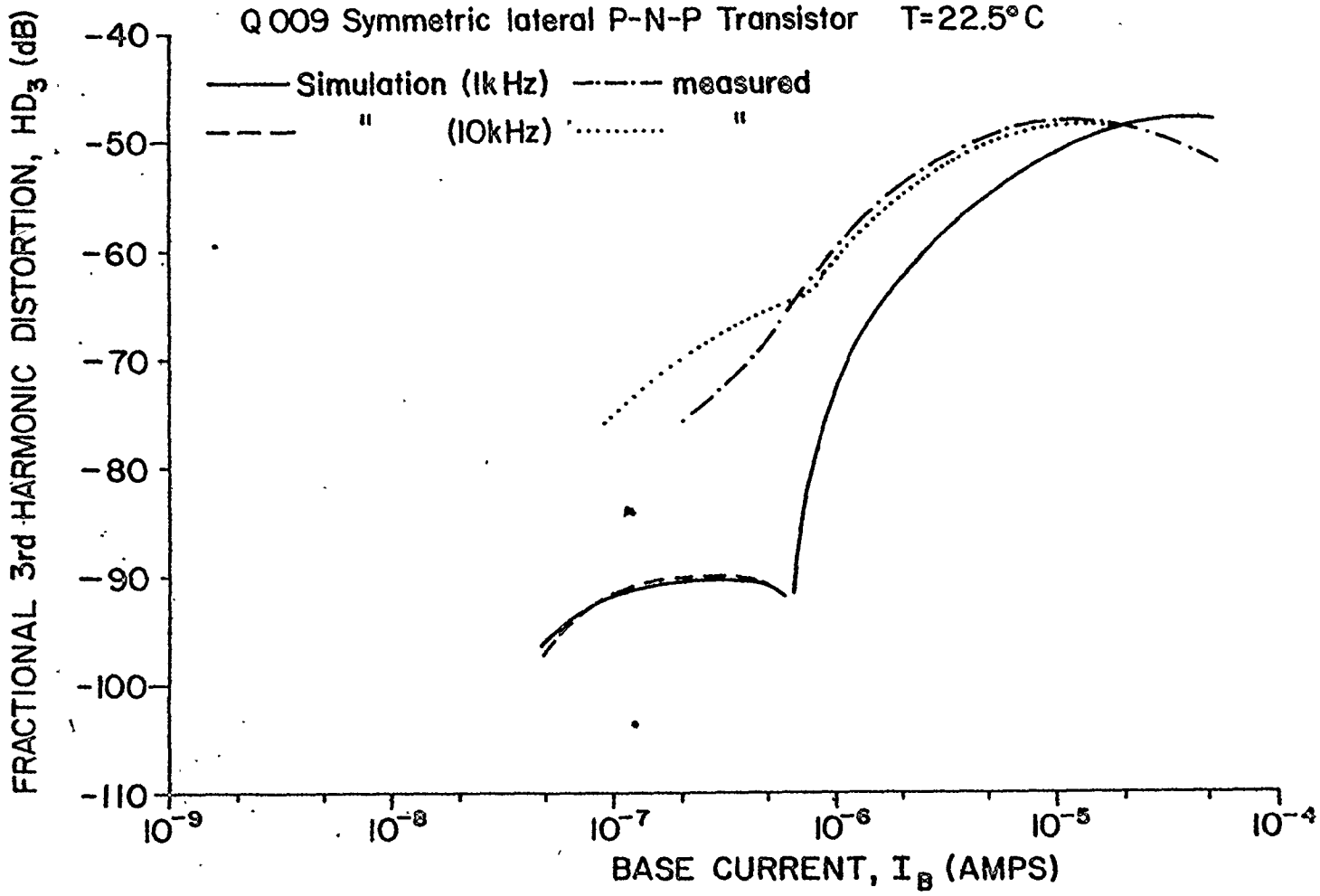

Figure 4.9. Fractional third harmonic distortion of the ZBT small-signal attenuator.

(4.10).

In order to determine the possible effects of a parallel resistance on g_2 and g_3, the 100 k Ω resistor of Figure 4.6 was replaced by a 10^{12} Ω resistor, effectively creating an open-collector condition. The simulated results for g_2 and g_3 were not found to change.

Computer simulation was also performed for the Q1 device, having parameters listed in Table 2.3. Due to the relatively small recombination components of I_B, the values of r_{eco}, g_2/g_{eco}, and g_3/g_{eco} were found to be very close to those predicted by (4.8)-(4.10), at low and moderate base currents.

4.3 Experimental Results

For the circuit of Figure 2.3, r_{eco} was measured in the manner described in Chapter Two. The base current was supplied by the calibrated current source of a Tektronix Type 576 curve tracer. The input signal was maintained at 4.24 mV rms.

The r_{eco} versus I_B characteristic measured for the Q009 device at 1 kHz is shown in Figure 4.1. Note the excellent agreement between the computer simulation and experimental results, even at high base currents. Similar measurements were made at 10 kHz; no change was found. Measurements were also made with the device operated in parallel with a fixed resistor R_p across the collector and emitter terminals. For values of R_p of 100 k Ω and 10 M Ω, the small-signal resistance of the combination was found, within the limits of experimental error, to be simply $(1/R_p + 1/r_{eco})^{-1}$. This supports the conclusion of Section

4.1.3 - that R_p does not affect the small-signal collector-emitter resistance of the ZBT if I_C is small.

Nonlinear distortion measurements were made with the Q009 transistor connected in the attenuator circuit of Figure 4.6. The substrate was biased at -2V with respect to the emitter. The input signal was supplied by a low-distortion Tektronix SG-505 oscillator; the base current was supplied by a Tektronix Type 576 curve tracer. Distortion products at the output were measured using a Hewlett-Packard 3580A Spectrum Analyzer. R_p was adjusted so that the parallel combination of R_p and the input impedance of the spectrum analyzer was 100 k Ω. The input signal was adjusted as I_B was varied, in order to maintain a constant value of v_o at the fundamental frequency. The values of HD_2 and HD_3 measured with an output signal of 10 mV rms at the fundamental are shown in Figures 4.8 and 4.9, respectively.

In order to ascertain the contribution of the base current source or the oscillator to the measured distortion, the ZBT was removed from the circuit, and the output of the current source fed directly into R_L. The value of v_o at the fundamental frequency was maintained at 10 mV rms as the base current was varied from 1×10^{-8} A to 1×10^{-4} A. No distortion products were detected within -90 dB of the fundamental component of v_o, the noise floor of the spectrum analyzer. Hence the results in Figures 4.8 and 4.9 can be attributed to the device itself.

The analysis of nonlinear distortion presented in this chapter assumes that the small-signal condition, as given by (4.63b), is satisfied. When this condition no longer holds, compression or

expansion of the fundamental component is observed. In the test circuit of Figure 4.6, v_i was increased in 10 dB steps and the corresponding change in v_o measured. This was found to be 10 $\pm$ 0.5 dB for values of v_o up to 31.7 mV. Similarly, the corresponding changes in HD_2 and HD_3 were 10 $\pm$ 0.5 dB and 20 $\pm$ 1 dB, respectively. Thus, the experimental data of Figures 4.8 and 4.9 are within the realm of nonlinear small-signal theory.

With reference to Figure 4.8, good agreement exists at 1 kHz between the simulated and measured values of HD_2 at moderate base currents. At lower base currents a discrepancy arises; at $I_B = 1 \times 10^{-8}$ A the measured value of HD_2 is almost 20 dB higher than the simulated value. This discrepancy is even greater at 10 kHz, where the theory and experiment are in agreement only above 10 μA. It is felt that this discrepancy is due chiefly to inaccurate modeling of the emitter-base and collector-base small-signal junction capacitances. From (1.7) and (1.8) these are, respectively,

$$C_{jE}(v_{EB}) = \frac{C_{jE}(0)}{\left[1 - \frac{v_{EB}}{\phi_E}\right]^{m_C}} \tag{4.78}$$

and

$$C_{jC}(v_{CB}) = \frac{C_{jC}(0)}{\left[1 - \frac{v_{CB}}{\phi_C}\right]^{m_C}} . \tag{4.79}$$

Ordinarily the junction capacitance is important only under reverse-bias and low forward-bias conditions, since under greater forward bias it is

much smaller than the small-signal diffusion capacitance. The three parameters associated with each junction capacitance are therefore usually obtained by fitting the capacitance versus voltage curve, measured with the junction reverse biased, to an expression of the form of (4.78) and (4.79) [6]. This can lead to very inaccurate results for the junction potentials ϕ_E and ϕ_C. In the case of the Q009 device ϕ_E and ϕ_C were found to be 0.5 V using this technique, whereas in actual fact they are of the order of 0.85 V for silicon devices.

Equations (4.78) and (4.79), which are included in SPICE, predict infinite capacitance at the point where the junction voltage equals the junction potential. Chawla and Gummel [21] have shown that (4.78) and (4.79) are not valid near this point. Instead, the junction capacitances reach a finite maximum, then decrease sharply for junction voltages greater than the junction potential. The program SPICE avoids the problem of infinite capacitance by approximating C_{jE} and C_{jC} as linear functions for $v_{EB} > N\phi_E/2$ and $v_{CB} > N\phi_C/2$, where $0 < N < 2$. The parameter N is set by the user. This is generally acceptable in first-order small-signal analyses, since under forward bias the junction capacitances are small in comparison with the diffusion capacitances. However, nonlinearities in C_{jE} and C_{jC} are completely ignored. Since C_{jE} and C_{jC} are in actual fact highly nonlinear functions of the junction voltages, their contribution to device nonlinearity is expected to be significant at high frequencies.

In the simulation performed for the Q009 device, N was set equal to one. As a result, the contributions of the junction capacitances to

HD_2 and HD_3 were neglected for junction voltages greater than 0.25V. While it is possible to increase N, this is of little value if ϕ_C and ϕ_E are not known with accuracy. Even if N = 2, the nonlinear behaviour of the junction capacitors of the Q009 device is neglected for junction voltages greater than 0.5 V. For $v_{CB} < N\phi_C/2$ and $v_{EB} < N\phi_E/2$ the predicted nonlinear behaviour is correct only if ϕ_E and ϕ_C, and hence the capacitance-voltage relationships (4.78) and (4.79), have been accurately determined. Precise measurements of ϕ_E and ϕ_C can be made using procedures more elaborate than the reverse-bias curve-fitting technique. It is felt that this would result in better prediction of the frequency-dependent nonlinear behaviour of the ZBT.

The effect of a finite base-drive impedance on device nonlinearity, discussed in Section 4.1.4, must also be considered as a possible explanation for the discrepancy between the measured and simulated values of HD_2 at low base currents. At $I_B = 1 \times 10^{-8}$ A the output impedance of the base current source was found to be approximately 50 M Ω. Through computer simulation the magnitude of HD_2 was found to increase by 5 dB at $I_B = 1 \times 10^{-8}$ A over the simulated value shown in Figure 4.8, which was obtained for an ideal current source. This is insufficient to account for the discrepancy of almost 20 dB between the measured and simulated curves. At higher base currents, the simulated effect of the current source on HD_2 was found to be negligible.

From Figure 4.9 it is apparent that the measured HD_3 versus I_B curves are nearly identical at 1 kHz and 10 kHz, except at low base

currents. Hence the offset between the theoretical and simulated curves cannot be attributed solely to inaccurate modeling of the junction capacitances. It is likely also due to the sensitivity of g_3/g_{eco} to the recombination parameters of the model equations. With reference to (4.25), even very small errors in n and C_B result in a significant error in g_3/g_{eco}, and hence in HD_3. The effects of the finite output impedance of the base current source on HD_3 were simulated, and found to be negligible over the range of base currents for which HD_3 was measured.

CONCLUSION

A modified version of the integral charge control model of Gummel and Poon has been used to investigate the ac and dc characteristics of the saturated bipolar transistor, in the situation where I_C is zero or close to zero. Analytic expressions have been obtained for the dc collector-emitter voltage, the ac small-signal conductance, and second and third-order small-signal nonlinear distortion in terms of the base current and the device parameters. The validity of these expressions has been established through computer simulation.

At low base currents the ac and dc characteristics are found to be dominated by carrier recombination within the junction space-charge layers and at the surface. At high base currents high level injection and the collector and emitter series resistances dominate device behaviour. From the standpoint of practical applications, optimum performance for a given device is achieved at moderate base currents, where recombination and high-current effects are negligible. In this region V_{ECO} and the small-signal nonlinear terms g_2/g_{eco} and g_3/g_{eco} are minimized, and are independent of I_B, while the small-signal conductance g_{eco} varies linearly with I_B. With proper fabrication it should be possible to produce a ZBT having these characteristics over several decades of I_B. It is shown that a device having symmetric forward and reverse-active mode parameters exhibits substantially less second and third-order nonlinearity than a conventional device, for which $\beta_F >> \beta_R$

and $C_2 >> C_4$. Thus, the optimum structure for a ZBT is markedly different from that required for typical high-gain transistors. The symmetric device is also found to be superior to a parallel configuration of two conventional devices, in terms of both ac and dc performance.

The parasitic substrate transistors are shown to have a significant effect on the behaviour of the ZBT, and must be included in the model if accurate results are to be expected. In general, the effects of the substrate can be reduced through appropriate processing techniques.

The behaviour of the ZBT in various circuit configurations has also been examined. The results of Section 4.1.3 show that a fixed resistance in parallel with the ZBT has no significant effect on its small-signal characteristics, if the dc collector current is small. The dc collector-emitter voltage decreases with respect to its open-circuited value at low base currents. The results of Section 4.1.4 indicate that the output resistance of the current source supplying I_B can increase the small-signal device nonlinearity if it is sufficiently low.

A number of applications for the ZBT have been suggested, particularly in situations where a small-signal variable-impedance element is required. Its small size and low current requirements make it ideally suited for low-voltage micropower circuits. A perturbation method has been used to analyze a small-signal attenuator and a variable-gain feedback amplifier incorporating the ZBT. Expressions

have been obtained for the second and third harmonic distortion components of the output signal in terms of the circuit parameters, the input voltage, and the small-signal characteristics of the ZBT. This technique can be applied to circuits of arbitrary complexity.

Experimental data were obtained for a family of symmetric lateral p-n-p transistors. The measured and theoretical values of V_{ECO} are in excellent agreement at low and moderate base currents. At very high base currents a discrepancy is observed. It is felt that this can be attributed to high-current effects not included in the model, in particular conductivity modulation in the active base region. A detailed investigation of these effects would undoubtedly lead to a better understanding of the dc behaviour of the ZBT in the high-current region. The predicted values of the small-signal resistance are in excellent agreement with the measured data, even at high base currents. Thus, the phenomena giving rise to the discrepancy noted above do not appear to have a significant effect on the small-signal behaviour of the ZBT.

At moderate base currents the predicted and measured values of small-signal second-order distortion are in good agreement, with a discrepancy arising at lower currents. This is more marked at higher frequencies. It is felt that more accurate measurements of the junction potentials would result in better agreement, since these parameters critically influence the behaviour of the nonlinear small-signal junction capacitances.

The third-order small-signal characteristics of the ZBT have been

found to be less sensitive to frequency-dependent nonlinearities than those of the second order. The theoretical curve of HD_3 versus I_B qualitatively accounts for the features of the measured curve, although there is a significant offset between the two. This is felt to be a result of the sensitivity of g_3/g_{eco} to small errors in the recombination parameters.

The results presented in this paper have provided a sound basis for future study of the ZBT. Possible areas of further research include an investigation of the effects of base current modulation on the ac and dc device behaviour, and an examination of the noise characteristics of the ZBT. A better understanding of the device would undoubtedly encourage its application in a wide variety of circuits.

REFERENCES

1. R.S. Hughes, "Semiconductor Variable Gain and Logarithmic Video Amplifiers." Phoenix: The Continuing Education Institute, 1967.

2. M.J. Howes and D.V. Morgan, ed., "Variable Impedance Devices." New York: Wiley, 1978.

3. H.K. Gummel and H.C. Poon, "An Integral Charge Control Model of Bipolar Transistors," Bell Syst. Tech. J., Vol. 49, pp. 827-851, May, June 1970.

4. L.W. Nagel and D.O. Pederson, "Simulation Program with Integrated Circuit Emphasis (SPICE)", 16th Midwest Symposium on Circuit Theory, Waterloo, Ontario, April 12, 1973.

5. L.W. Nagel, "SPICE2: A Computer Program to Simulate Semiconductor Circuits," Electronics Research Laboratory Report No. ERL-M520, University of California, Berkeley, 9 May, 1975.

6. I.E. Getreu, "Modeling the Bipolar Transistor." New York: Elsevier, 1978.

7. C.T. Sah, "Effect of Surface Recombination and Channel on p-n Junction and Transistor Characteristics," IRE Trans. Electron Devices, Vol. ED-9, pp. 94-108, Jan. 1962.

8. C.A. Bittman, G.H. Wilson, R.J. Whittier and R.K. Waits, "Technology for the Design of Low-Power Circuits," IEEE J. Solid-State Circuits, Vol. SC-5, pp. 29-37, Feb. 1970.

9. R. Beaufoy and J.J. Sparkes, "The Junction Transistor as a Charge-Controlled Device," ATE J., Vol. 13, pp. 310-324, Oct. 1957.

10. H.H. Berger, "The Injection Model - A Structure-Oriented Model for Merged Transistor Logic (MTL)," IEEE J. Solid State Circuits, Vol. SC-9, pp. 218-227, Oct. 1974.

11. H.H. Berger and Uta Dreckmann, "The Lateral P-N-P Transistor - A Practical Investigation of the DC Characteristics," IEEE Trans. Electron Devices, Vol. ED-266, pp. 1038-1046, July 1979.

12. M.J. Callahan, "Models for the Lateral P-N-P Transistor Including Substrate Interaction," IEEE Trans. Electron Devices, Vol. ED-19, pp. 122-123, Jan. 1972.

13. P.E. Gray, D. DeWitt, A.R. Boothroyd, and J.F. Gibbons, "Physical Electronics and Circuit Models of Transistors," SEEC Vol. 2. Wiley: New York, 1964.

14. J. Choma, "Error Minimization in the Measurement of Bipolar Collector and Emitter Resistances," IEEE J. Solid-State Circuits, Vol. SC-11, pp. 318-322, April 1976.

15. A.Z. Incecik, "Computer-Aided Determination of Emitter and Collector Resistances of Integrated Bipolar Transistors," IEEE J. Solid-State Circuits, Vol. SC-14, pp. 1108-1110, Dec. 1979.

16. C.T. Sah, R.N. Noyce and W. Shockley, "Carrier Generation and Recombination in P-N Junctions and P-N Junction Characteristics," Proc. IRE, Vol. 45, pp. 1228-1243, Sept. 1957.

17. E. Wildi, J.W. Knutti, and J.D. Meindl, "A Micropower, Small Input-to-Output Delay, High-Voltage Bipolar Driver/Demultiplexer IC," IEEE J. Solid-State Circuits, Vol. SC-16, pp. 23-29, Feb. 1981.

18. Y.L. Kuo, "Distortion Analysis of Bipolar Transistor Circuits," IEEE Trans. Circuit Theory, Vol. CT-20, pp. 709-716, Nov. 1973.

19. S.H. Chisholm and L.W. Nagel, "Efficient Computer Simulation of Distortion in Electronic Circuits," IEEE Trans. Circuit Theory, Vol. CT-20, pp. 742-745, Nov. 1973.

20. W.J. Cunningham, "Introduction to Nonlinear Analysis." New York: McGraw-Hill, 1958.

21. B.R. Chawla and H.K. Gummel, "Transition Region Capacitance of Diffused P-N Junctions," IEEE Trans. Circuit Theory, Vol. ED-18, pp. 178-195, March 1971.